Optics & Laser Technology 146 (2022) 107595

Contents lists available at ScienceDirect

Optics and Laser Technology

journal homepage: www.elsevier.com/locate/optlastec

A review on dissimilar laser welding of steel-copper, steel-aluminum, aluminum-copper, and steel-nickel for electric vehicle battery manufacturing

Amirhossein Sadeghian *, Naveed Iqbal

Institute for Advanced Manufacturing and Engineering, Coventry University, CV6 5LZ, UK

ARTICLE INFO

Keywords:
Laser welding
Electric vehicle battery
Steel
Copper
Aluminium
Nickel

ABSTRACT

The electric vehicle (EV) battery systems are complex assemblies of dissimilar materials in which battery cells are connected using several thousand interconnect joints. Every single joint influences the functionality and efficiency of the whole battery system, making the joining process crucial. Laser welding is considered a desirable choice for EV battery manufacturing due to its non-contact nature, high energy density, precise control over the heat input, and ease of automation. However, incompatible thermos-physical properties of dissimilar materials used in battery tabs and interconnectors pose a significant challenge for achieving complete metallurgical bond. Furthermore, the formation of undesirable weld microstructures such as hard and brittle intermetallic compounds (IMCs) substantially undermines the structural, electrical, and thermal characteristics of battery joints. This paper reviews the fundamental difficulties and latest developments in dissimilar laser welding of steel-copper, steel-aluminum, aluminum-copper, and steel-nickel, some of the potential joint combinations in EV battery pack manufacturing. The weld microstructure and common metallurgical defects, as well as mechanical and electrical properties of joints are discussed. In addition, the effects of laser welding process parameters on the joint properties and the applicability of various interlayers and coatings in laser welding of battery materials are assessed.

1. Introduction

The transport sector accounts for 24% of global CO_2 emissions due to the combustion of fossil fuels [1]. It has been reported that internal combustion engine (ICE) vehicles are responsible for almost three-quarters of this amount [2]. Under this threatening situation, carbon emission legislations have been set out across the globe to mitigate the harmful effects of climate change [3,4]. Such policies have prompted nations to modernize the automotive sector and develop electric vehicles (EVs) to decrease their carbon footprint [5]. The UK, for example, plans to ban the sale of new petrol and diesel cars from 2030 and bring all greenhouse gas emissions to net-zero by 2050 [6]. Similar targets have been set by other major industrialized countries such as China and the EU [7,8].

Although EVs offer a promising alternative to conventional vehicles, they only accounted for 2.6% of global car sales and about 1% of the entire global car stock in 2019 [9,10]. The fundamental barrier to the large-scale adoption of EVs is the limited driving range which combined with insufficient charging infrastructure can lead to “range anxiety” in EV drivers [11–13]; the fear of stranding with an empty battery [14]. Currently, most EVs can only go around 100–250 km on a single charge, much shorter than their ICE counterparts [15]. Using larger batteries is not a feasible solution owing to limited space in EVs, additional cost, higher weight, and the requirement of more rare-earth elements [16,17]. Hence, there is a need to enhance the energy density of the existing battery system as the key component that determines the vehicle’s performance [18,19].

Currently, lithium-ion solid-state batteries are the most commonly used source of power for many low to high-capacity applications, including portable electronics and EVs [20]. While in mobile devices such as cell phones and laptops only a handful of cells are required, up to several thousand cells are inter-connected in EV battery systems to deliver the necessary power. Thus, the cell-to-cell or module level joining is the most critical joining process in battery pack manufacturing which directly influences the battery capacity [21]. The overview of the EV battery pack consisting of cell, module, and pack structure is

* Corresponding author.
E-mail address: sadeghiana@uni.coventry.ac.uk (A. Sadeghian).

https://doi.org/10.1016/j.optlastec.2021.107595
Received 16 May 2021; Received in revised form 17 August 2021; Accepted 5 October 2021
Available online 18 October 2021

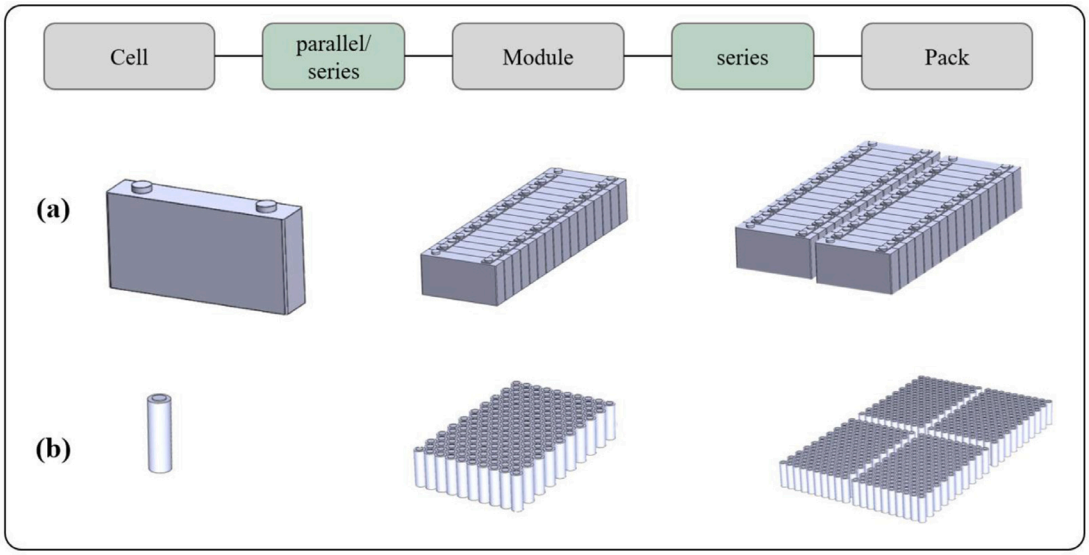

Fig. 1. The EV Battery pack overview with (a) prismatic cells (b) cylindrical cells [21].

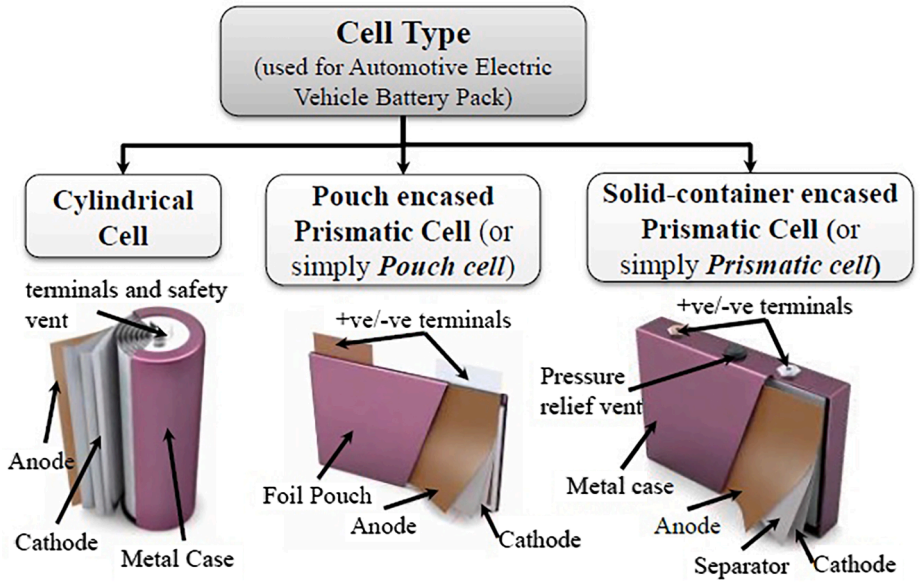

Fig. 2. Cell types commonly used in EV battery pack [20].

illustrated in Fig. 1.

EV batteries currently use three cell formats: cylindrical, prismatic, and pouch cells [20,22]. Fig. 2 shows these three cell formats [20]. Welding occures in all of them. For example, in the pouch format, the cell tabs are usually made of aluminum or copper and are generally connected in parallel or series configurations using steel, aluminum, copper or nickel busbars [21]. Weld joints in EV battery pack involve low-thickness materials (typically 0.3 mm to 1 mm) and the welding process is normally performed in lap, fillet, or spot configuration [23,24]. A typical joint between Al tab to Cu busbar in pouch cells is presented in Fig. 3 [25]. The differences in thermos-physical properties of dissimilar materials such as melting temperature and thermal conductivity make it difficult to obtain a complete metallurgical bond without considerable cracks and porosities [26]. Furthermore, the formation of hard and brittle intermetallic compounds (IMCs) at the weld interface greatly reduces the battery's electrical capacity and structural performance. A weak joint cannot withstand the harsh driving environments, dynamic loading, vibrations, and possible crash and might even result in fire due to short-circuiting [27,28]. The presence of IMCs also intensifies the heat generated during charging and discharging cycles due to their low electrical conductivity thereby accelerating the degradation process of the battery. The possibility of corrosion due to the presence of IMCs which further deteriorates the joint performance should be considered as well [29]. Atmospheric, localized, crevice, pitting, and galvanic are the most known types of corrosion that can happen here [30]. Corrosion not only degrades the mechanical performance of joints but it can also increase the connection electrical resistance [31]. In summary, a proper joint in the EV battery system must satisfy the following requirements:

- Low electrical resistance
- Good strength
- High fatigue resistance
- Low corrosion risk [32,33].

Wire bonding (WB), resistance spot welding (RSW), ultrasonic

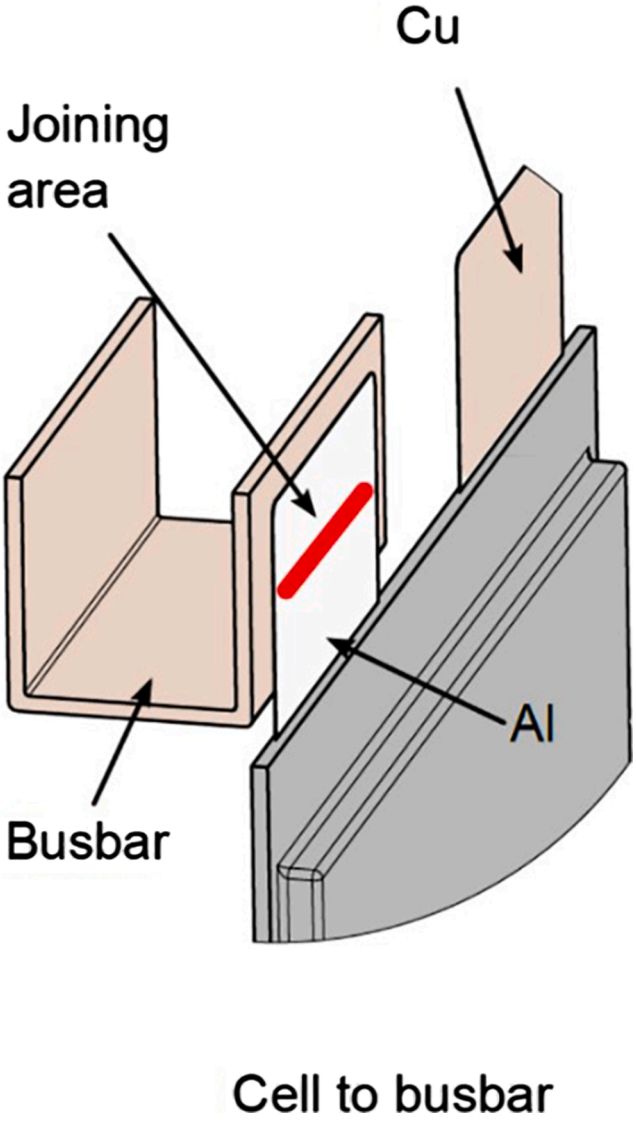

Fig. 3. Joining of Al tab to Cu busbar in pouch cells [25].

welding (UW), and laser welding (LW) are the most investigated joining techniques for EV battery manufacturing [21]. Each of these methods has its advantages and limitations and is used based on cell type, properties, and thickness of the materials involved [20]. Other joining processes such as soldering, friction stir welding, micro-TIG or pulsed arc welding, joining by forming, and adhesive bonding have also been proposed [34–38]. However, due to the lack of information at present, further research is needed to thoroughly assess their feasibility [21].

In ultrasonic welding, a high-frequency (typically 20 kHz or above) ultrasonic vibration is applied under pressure to join substrates [20]. Oxides and contamination on the surfaces are removed during the welding and the result is a metallurgical bond created without melting, based on diffusion and adhesion of the softened metals [39,40]. UW can

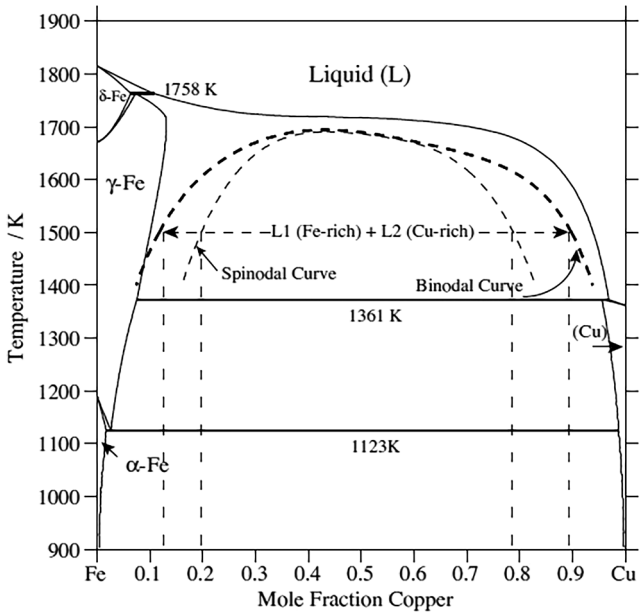

Fig. 4. The binary Fe-Cu Phase diagram showing the metastable miscibility gap (i.e., binodal curve) [50].

produce good welds (without porosity, hot-cracks, and bulk intermetallics) between highly conductive dissimilar metals, and has been considered particularly superior for pouch cells. However, it can damage the structural integrity of cylindrical and prismatic cells due to the high frequency of vibration. It is also restricted to lap joints [20]. Wire bonding can be defined as single-sided ultrasonic welding of a small diameter Ag, Cu, or Al wire (typically below 0.5 mm), first to one substrate and then to the second or more substrates sequentially [22]. It is a technique frequently used in semiconductor device technology [21], and regardless of no scientific literature on its application in EV battery manufacturing, wire bonding has been employed in Tesla Model-S to connect battery cells and busbars [20]. Resistance spot welding is another method that can be used for EV battery welding. When a high current passes through the interface, it creates localized heating and melting, resulting in fusion welding of substrates [41]. However, resistance spot welding of highly conductive materials like aluminum and copper remains challenging and currently, this process is only suitable for low-conductivity materials [20,42]. Laser welding is a highly efficient fusion welding technique with the advantages of creating a narrow heat-affected zone and a small targeted deformation [43]. Compared to other main welding techniques for EV battery pack manufacturing (i.e., RSW and UW), the lowest electrical contact resistances and highest joint strengths have been reported with laser welding [44]. Laser welding has the potential to be used for all three types of lithium-ion cells [20]. However, A poor metallurgical affinity between dissimilar materials normally limits the laser welding process and leads to potential defects such as the formation of detrimental intermetallic phases and crack sensitivity. Studies so far have reported that the joint performance could be improved by optimizing the welding process parameters [45]. Furthermore, the applicability of different interlayers and coatings to improve joint properties has been the subject of some recent

Table 1
Summary of the room temperature properties of Al, Cu, Fe, and Ni [49].

Metal	Melting Temperature (K)	Boiling Temperature (K)	Density (Kg m^{-3})	Thermal Conductivity (W m^{-1} K^{-1})	Specific Heat Capacity (J Kg^{-1} K^{-1})	Thermal Expansion Coefficient (10^6 K^{-1})
Fe	1809	3133	7870	78	456	12.1
Al	933	2793	2700	238	917	23.5
Cu	1356	2833	8930	397	386	17
Ni	1728	3188	8900	89	452	13.3

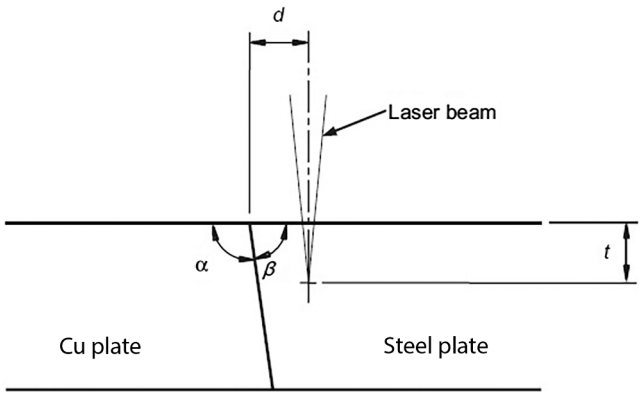

Fig. 5. The Scheme of butt configuration weld between Cu and steel plate with a scarf geometry [55].

investigations [46]. There have also been advances in novel lasers (i.e., blue and green lasers) which allow higher energy absorption on highly reflective surfaces of metals such as Cu and Al [47,48].

This paper presents a comprehensive review on the dissimilar laser welding of the most common joint combinations in EV battery system including steel-copper, steel-aluminum, aluminum-copper, and steel-nickel. The fundamental metallurgical and structural challenges are discussed and the latest developments in process optimization have been highlighted to provide a basis for further studies on this topic.

2. Steel-copper

The welding of steel to copper is quite common when connecting cells in EV battery systems especially in cylindrical format. Table 1 presents the room temperature properties of Al, Cu, Fe, and Ni. While the data is for pure metals, they are still useful in understanding the differences in thermos-physical properties of their respective alloys. The differences in melting temperatures and thermal conductivities make obtaining a complete metallurgical bond very challenging in these systems [49]. In Fe and Cu phase diagram, there is a wide metastable miscibility gap at high temperatures (Fig. 4 [50]). Separation of the liquid phase is a common feature in laser welding of steel and copper due to rapid solidification, as undercooled Fe-Cu liquid separates into droplets of iron and copper [51]. Another major problem is hot cracking in the weld zone or heat-affected zone (HAZ) of steel owing to Cu penetration into the grain boundaries [52].

Autogenous butt joints between steel and copper have been the subject of several investigations. Most of these studies focused on laser welding of stainless steel and pure copper. It has been suggested by some authors that the key to a high-quality joint between copper and steel is reducing the intermixing of molten steel and copper by keeping the Cu in solid-state, mainly by using laser beam offset or beam deflection towards the steel side. This suppresses the metastable phase separation during welding, thereby preventing weld cracks and HAZ microfissures [53–55]. Mai and Spowage [45] produced butt joints between 1 mm medium carbon tool steel and copper by focusing the beam 0.2 mm towards steel in order to minimize the melting of Cu. While the top of steel completely melted a lack of fusion was observed between Cu and the weld metal. They suggested preheating the joint or using a higher power density as possible solutions which can improve the joint quality. Yao et al. [55] proposed a scarf geometry (i.e., obtuse and acute angles for copper and steel, respectively) for the butt weld configuration with the laser offset towards steel. Fig. 5 shows the schematics of this proposed scarf geometry. Plane thickness and laser power had important effects on the distribution of Cu. Higher thickness (10 mm) and laser power (11kW) reduced the amount of molten copper dissolved in steel

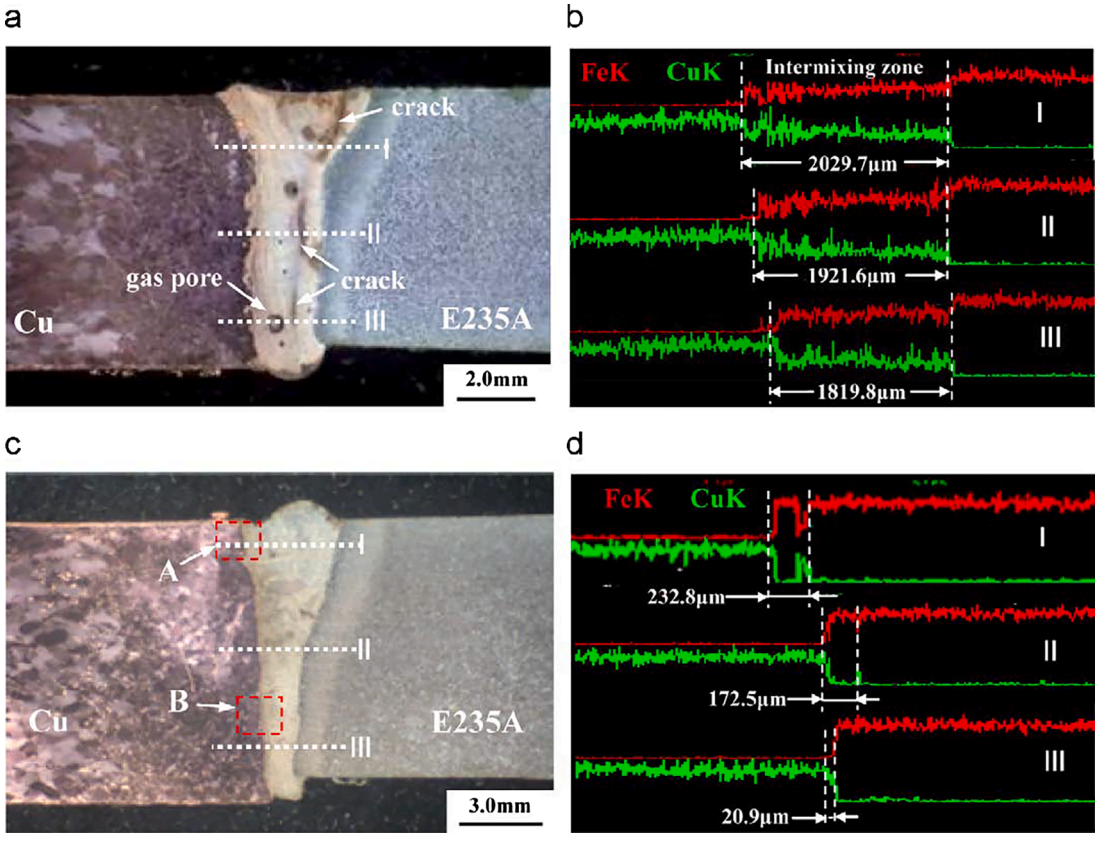

Fig. 6. a) Microstructure of the joint with a higher Cu dilution (~36 at.%), b) EDS line scans of Fe(K) and Cu(K), c) microstructure of the joint with a lower Cu dilution (<1 at.%), d) EDS line scans of Fe(K) and Cu(K) [55].

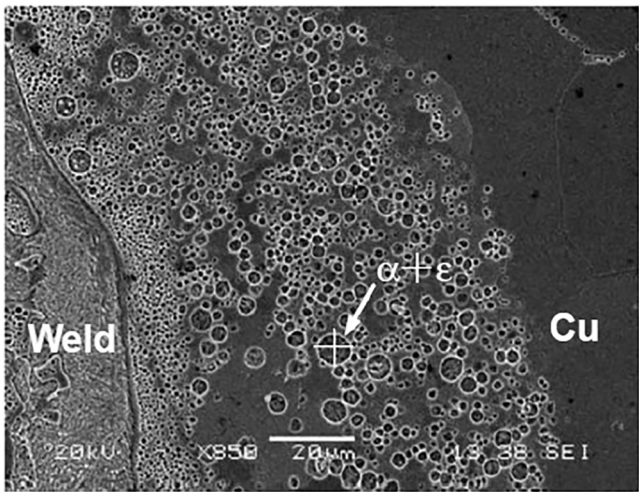

Fig. 7. Microstructure near the interface between intermixing zone and Cu plate [55].

compared to the sample with a thickness of 7 mm and a laser power of 8 kW. Fig. 6a and b illustrate the cross-sectional morphology of joints with a high dilution ratio of Cu (~36 at.%) and the corresponding EDS intensity profiles of Fe and Cu. The morphology and EDS profiles of the low-dilution (<1 at.%) sample are presented in Fig. 6c and d, respectively. A complete metallurgical bond without cracks and pores along with a higher tensile property was achieved for the low-dilution sample. Cracks and gas pores can be seen in the high-dilution sample which showed a tensile strength of only 150–200 MPa. An intermixing zone existed adjacent to the Cu plate in both samples. However, it was narrower in the low-dilution sample owing to the lower diffusion of Cu. This transition zone consisted of a large number of granular phases with a composition of Fe-rich bcc solid solution (α-Fe) and Cu-rich fcc solid solution (known as the ε phase) (Fig. 7).

Chen et al. [53,56] have reported the microstructural characteristics of laser-welded stainless steel to copper, using an oblique angle. They stated that laser beam inclination towards the stainless steel could melt it while keeping the low-melting-point copper in solid-state, resulting in the "welding-brazing mode". Owing to the low amount of melted Cu it forms a dilute solution in the fusion zone. However, excessive beam offset or welding speed should be avoided since they can result in the lack of fusion in the copper and the weld zone interface. While in "welding-brazing mode", liquid separation and microcracks in the fusion zone were prevented, in "fusion welding mode" the melt pool entered the metastable miscibility gap and separated into two immiscible liquids of Cu and stainless steel. These two joining modes are shown in Fig. 8.

A jagged interface was formed between copper and liquid metal owing to the strong fluid flow of the molten pool during the welding. The composition distribution at the interface during welding-brazing is presented in Fig. 9. The diffusion of alloying elements of stainless steel (e.g., Fe, Cr, Mn, and Ni) into copper is an indication of a metallurgical bond between copper and stainless steel. The combination of scraggly interfacial morphology and metallurgical bonding resulted in improved mechanical properties in the "welding-brazing" mode.

In "fusion welding mode" when partial melting of copper and mixing with the melt pool occurred, the liquid underwent primary and secondary separation owing to the high cooling rate and supercooling of the laser welding process. Fig. 10 illustrates the mechanism of liquid separation in "fusion welding mode". Instantly after entering the miscibility gap the liquid underwent the primary separation creating Fe and Cu liquids. With the lack of full diffusion, the secondary liquid phase separation occurred as the liquid cooled in the miscibility gap resulting in the supersaturation of one or both liquids. The final weld microstructure was an inhomogeneous composite of Cu and stainless steel.

Fig. 11 shows the presence of cracks at the weld zone in "fusion welding mode". These cracks are believed to be caused by a thermal stress mismatch between stainless steel and copper. It can be seen that copper filled some of these cracks due to its low melting temperature. A metallurgical bond was formed between the crack surfaces and molten copper creating a self-healing property thereby reducing the negative effects of cracks. Since some of the cracks were filled with molten copper the tensile strength was not influenced by the presence of these cracks. Nevertheless, the toughness and fatigue strength decreased with the increase in the amount of molten copper. Thus, it was concluded that the

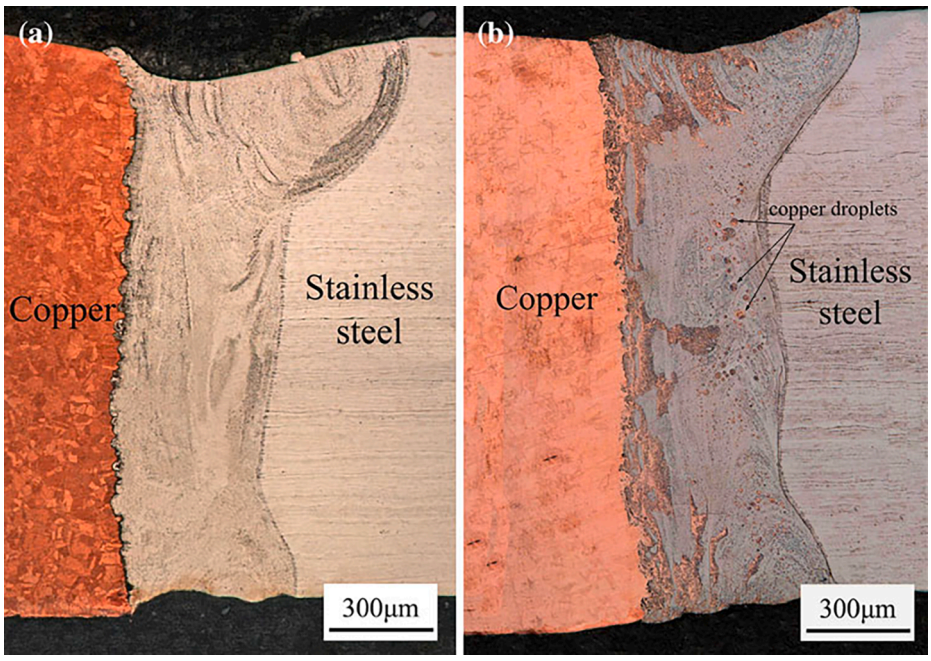

Fig. 8. (a) "welding-brazing mode" (beam inclination 0.2 mm towards steel), (b) "fusion welding mode" (without beam inclination) in laser welding of copper and stainless steel [53].

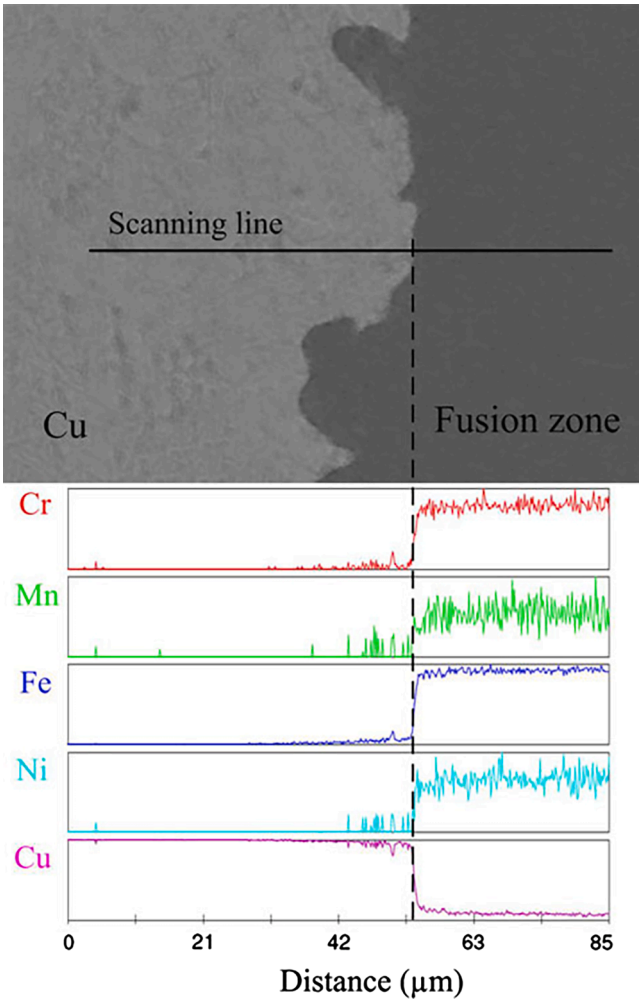

Fig. 9. Composition distribution at the interface between copper and stainless steel in "welding-brazing mode" [53].

melting of Cu should be kept at a minimum.

Li et al. [57] declared HAZ liquation cracking in the stainless steel and fusion zone porosities as the two major defects in laser welding of stainless steel and copper. The existence of Fe-Cu compounds at the HAZ grain boundaries weakened the cohesion between grains and created the susceptibility to cracks. The three stages of liquation cracking formation are presented in Fig. 12. The first stage is crack incubation at grain boundaries in which Cu atoms permeated along the grain boundaries due to a small resistance. In the second stage, crack initiation, Fe-Cu compounds enriched at grain boundaries undermining the cohesion between the grains. Crack growth is the third and final stage. The thermal stresses increased massively with the increase in heat input during the laser welding process, leading to the extension of small cracks into forming big cracks at grain boundaries.

Fig. 13 illustrates the relationship between heat input and crack length. The crack length was increased with increasing the heat input till 125 kJ/m, after which it began to fall. This was attributed to the self-healing property of molten copper which filled the cracks. It was believed although crack susceptibility could be lowered with self-healing, to control the weld quality the heat input should be reduced by increasing the welding speed or by lowering the laser power. The other major problem, porosities, occurred independently of HAZ liquation cracking. These porosities were the results of keyhole instability correlated with the fluid flow. They were successfully removed by beam deflection towards stainless steel that altered the flow of liquid metal and increased the stirring effect during the welding process [57].

Kuryntsev et al. [58] laser welded 321 stainless steel and copper by using a stainless steel lead-in plate to keep the Cu in a solid state. By using this method, no cracks or pores were found in the weldments. The electrical resistance of the welds was also measured which was more than two times lower than that of stainless steel, indicating a lack of intermetallics in the weld zone. Other researchers have also reported obtaining sound welds without defects between stainless steel and copper by minimizing the melting of copper either using beam offset or inclining the laser beam towards stainless steel [59–62].

Contrary to above investigations, an alternative approach has been explored by researchers such as Shen and Gupta [63]. In their study, beam was put towards Cu in laser welding of 316 stainless steel to oxygen-free copper. They reported that laser welding with the beam focused on the steel side always led to solidification cracks in the weld zone no matter the welding parameters. Therefore, a focus of 0.4 mm towards Cu was used. They reported that when weld metal was enriched with copper (80% of copper in the weld zone) no solidification cracks were detected. Hot crack clusters were observed along the austenite grain boundaries in stainless steel-HAZ. However, a high tensile strength of 312 MPa was achieved despite the presence of these cracks. Sahul et al. [64] achieved high values of tensile strength up to 261 MPa by offsetting the laser beam towards the copper side due to intermixing of both metals. The microstructure of the welds between AISI 304 and Cu is presented in Fig. 14. Fine copper dendrites can be observed at the interface between weld and copper. The interface was also jagged indicating metallurgical bonding. Grain growth was observed in the HAZ of copper. Furthermore, δ ferrite was detected at the interface of stainless steel and weld metal. Elemental mapping of Cu, Cr, Fe, and Ni are illustrated in Fig. 15. Visible intermixing of elements can be seen, dark zones originating from 304 stainless steel and brighter ones from Cu.

Similarly, Weigl and Schmidt [65] and Joshi and Badheka [66] reported the presence of the solidification cracks in the "welding-brazing mode". It was concluded that the presence of Cu within the weld metal was not responsible for the solidification cracks, and by shifting the beam towards the Cu a higher amount of Cu was melted and participated in the weld resulting in better static mechanical strength. They believed beam displacement was not the only way to control solidification cracks. Since compositional gradient within the weld area was the reason for the cracking, detail works on welding parameters are needed to investigate the interaction of stainless steel and copper within the weld metal and its effect on solidification cracks.

Lap laser welding between steel and Cu has been the subject of a number of studies. Mehlmann et al. [67] studied the influence of modulation amplitude on laser welding of Ni-plated steel DC04 and bronze $CuSn_6$. By using a proper spatial modulation full penetration was achieved thereby maximizing the strength of the joints. Iqbal et al. [68] compared pulsed are welding (PAW) and laser welding for 0.3 mm Ni-coated copper and 0.7 mm mild steel. They used a novel beam wobbling process to control the weld penetration. Fig. 16 illustrates the effect of laser beam wobble frequency on the weld microstructure. Higher heat input in the sample with 200 Hz frequency resulted in complete dissolution of Ni coating while in the sample with 300 Hz frequency the interface was still visible. By comparing laser welding and PAW, it was observed that laser welding was able to produce joints with an efficiency of 93% while the weld efficiency for PAW was limited to 70%. Shaikh et al. [69] investigated laser welding of Ni-coated copper (Cu[Ni]) and Ni-coated steel (i.e., electrical grade Hilumin) in lap configuration. The effects of laser power, pulse on time, pulse frequency, and welding speed on the joint properties were studied. Penetration depth was increased with the increase in laser power. Laser power, pulse on time, and frequency had a positive correlation with the lap shear strength while speed exhibited a negative correlation. This was due to the fact that higher power, pulse on time, and frequency resulted in higher penetration and interface width. It was reported that the change in electrical resistance and temperature rise was relatively small in all

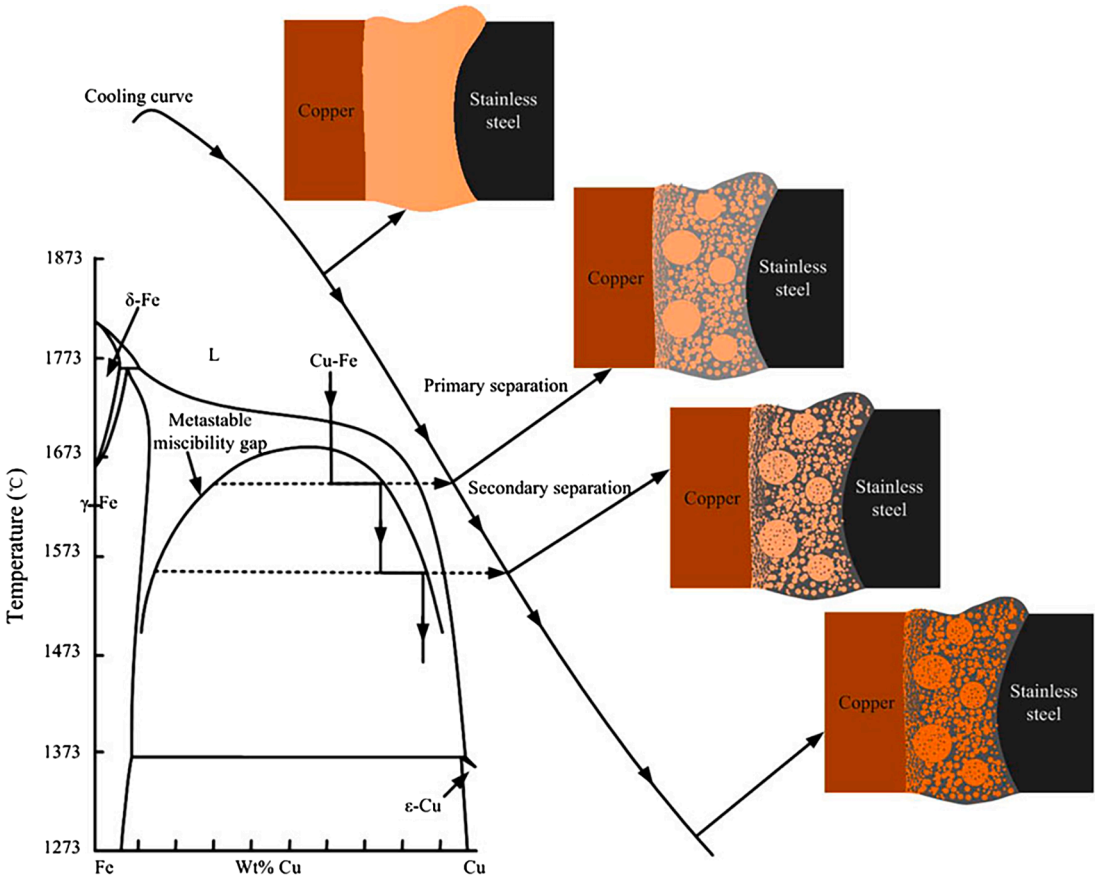

Fig. 10. Schematic of liquid separation and its mechanism in fusion welding of copper and stainless steel [53].

combinations of process parameters. With higher mixing of steel and copper higher strength was achieved while a slight increase in electrical resistance was observed (Fig. 17).

Table 2 gives a summary of research carried out on dissimilar laser welding of steel and copper. Mostly butt joint configuration between stainless steel and copper has been explored. However, further detailed metallurgical studies are necessary to determine the microstructure of the weld zone and the interaction between two materials. Besides, laser welding in lap configuration which is widely used in EV battery manufacturing needs more attention. The application of potential interlayers or coatings can also be the subject of future investigations.

3. Steel-aluminum

The fundamental challenge during laser welding of Al and steel is the formation of brittle intermetallics that usually include $FeAl_2$, Fe_2Al_5, and $FeAl_3$ [70]. Fig. 18 illustrates the equilibrium phase diagram of Fe-Al. The presence of these intermetallics reduces ductility and affects fatigue properties. Table 3 presents the hardness of intermetallic components of the Fe-Al system. It can be seen that Fe-rich intermetallics have much lower hardness compared to Al-rich intermetallics. The optimized heat input to control the melt pool geometry, cooling rate, and solidification parameters can potentially help to avoid the formation of the most detrimental intermetallic phases and improve the weld strength [71].

The data available in the public domain shows that several attempts have been made to control intermetallic formation through the optimization of process parameters, different heat source modes, and welding techniques. Torkamany et al. [70] laser welded the 0.8 mm thickness low carbon steel (ST14) to 2 mm thick aluminum alloy (AA5754), in the overlap configuration. They concluded that raising the laser power had an adverse effect and created more spatter and intermetallics. The weld microstructure exhibiting the presence of intermetallics at the bottom of the weld is shown in Fig. 19. Due to the formation of these intermetallics, crack propagation was observed in the weld metal and at the weld/Al interface. Increasing the pulse duration also had a similar effect as higher heat input resulted in the formation of a large number of intermetallic compounds. On the other hand, lowering the pulse duration below a critical level resulted in the lack of fusion. High welding speeds also resulted in incomplete fusion at the interface and reduced joint strength. They reported optimum values for process parameters that produced high-strength welds as a result of a low amount of intermetallics, high surface quality, and continuous interface layer without visible defects. This included a peak power of 1430 W, a pulse duration of 5 ms, and a welding speed of 4 mm/s.

Mathieu et al. [74] suggested that the formation of intermetallic phases (e.g., $FeAl_3$ and Fe_2Al_5) was not the only factor controlling the strength and ductility of the welds especially when their thickness is below 10 μm. Shrinkage pores and bad cohesion could be detrimental to joint strength. The global geometry of the welds should be taken into account too. There was a direct relationship between the length of the steel/weld seam and machinal strength. Indhu et al. [75] used a high-power, pulsed diode laser to join 3 mm thick aluminum alloy AA6061 with 2.5 mm thickness dual-phase steel DP600. They reported the formation of aluminum-rich intermetallics including Fe_2Al_5 and $FeAl_3$ at the weld zone. A laser power of 4 kW, scanning speed of 5 mm/s, and pulse duration of 10 ms reduced the thickness of intermetallics. In this case, the maximum intermetallic thickness of 7 μm and a minimum thickness of 1.03 μm was observed. Jin et al. [76] studied the effect of penetration depth on the mechanical properties of laser-welded stainless steel SS316L and pure aluminum. The joint was in lap configuration with steel on top. For the case of higher penetration depth, Al-rich

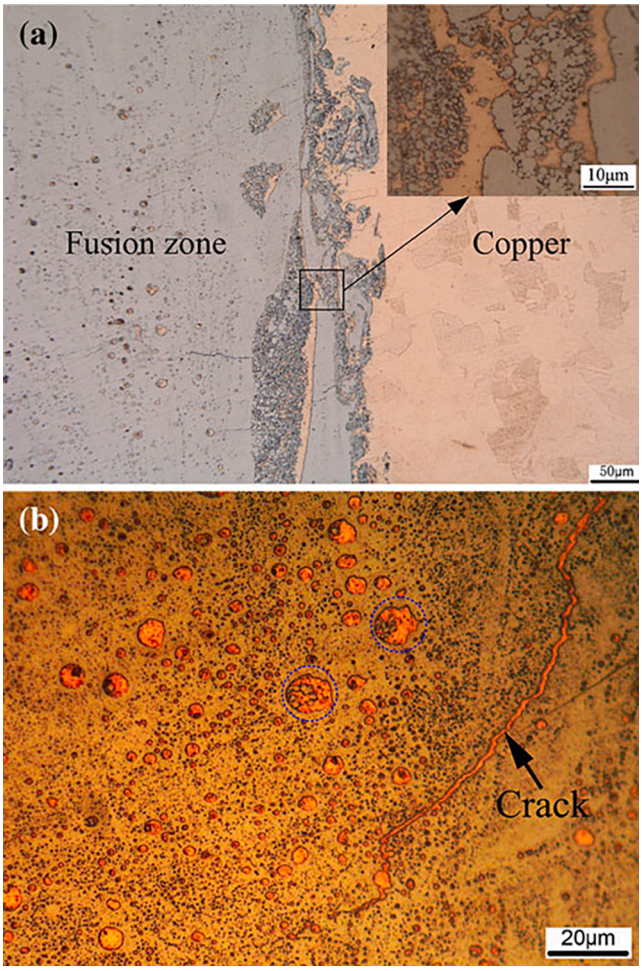

Fig. 11. Microstructure of the joint in "fusion welding mode" (a) at the interface, (b) at the fusion zone [53].

intermetallics were formed, while for low penetration depth Fe-rich intermetallics were observed without the presence of any defects thereby enhancing the mechanical properties of the joints. Pereira et al. [77] investigated the optimal welding parameters based on mechanical and microstructural investigations. Two sheets of DP1000 steel and aluminum alloy AA1050 of 1 mm thickness were overlap-welded using a pulsed Nd:YAG laser. They reported good quality welds with tensile strengths close to parent AA1050 when laser power was low enough to prevent full penetration into Al. Laser welding of low carbon steel DC04 and aluminum alloy AA6016, both in 1 mm thickness, was investigated by Guan et al. [78] using a fiber laser. The focus of their study was to probe the impact of welding process parameters on the weld bead geometry and the tensile strength. They concluded that the welding speed was the main process parameter influencing the weld properties whereas beam defocus and laser power were secondary factors. Increasing welding speed reduced the Fe-Al reaction time leading to thinner intermetallics and improved the joint strength. The optimal laser welding parameter values were reported as laser power 1400 W, welding speed 40 mm/s, defocusing 0 mm, and gas flow 35 L/min. A two-pass laser process was utilized by Ma et al. [79] to produce laser welded joints between 0.75 mm DP590 galvanized steel and 1 mm 6061 aluminum. The first pass was intended to melt and partially vaporize the zinc coating whereas the second pass was executed to perform the welding. They declared that laser power and speed should be adjusted to vaporize the Zn coating but prevent creating extensive plasma. The best mechanical properties were achieved when the thickness of the Al-rich intermetallic layer was kept around 5 μm. Borrisutthekul et al. [80] investigated the impact of a backing plate (heat sink) in suppressing the formatin of intermetallics. Fig. 20 illustrates the dependence of weld strength on intermetallic thickness. As can be seen, the weld strength increased with the reduction of intermetallic thickness. They claimed that higher welding speeds and a backing plate with higher conductivity could reduce the thickness of the intermetallic layer leading to a higher weld strength. They used three different backing blocks; Ti, medium carbon steel (S45C), and Cu. The best result was achieved with the Cu backing block due to its higher conductivity which suppressed the generation of intermetallics owing to a higher solidification rate.

Similar results are reported by Pardal et al. [81] for the laser spot welding of steel to aluminum in the conduction mode. Welds produced with Cu backing plate had a much lower thickness of intermetallic layer compared to that of Al backing plate, leading to better mechanical properties. Yan et al. [82] compared a combination of continuous and pulsed dual-beam YAG laser with a single beam. Continuous-wave heated the materials and created the weld pool while pulse wave stirred the weld pool. Using this technique, the thickness of the

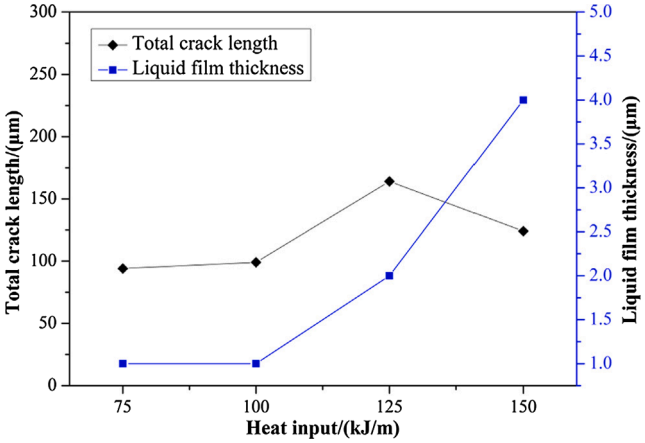

Fig. 13. The correlation between the total crack length and heat input [57].

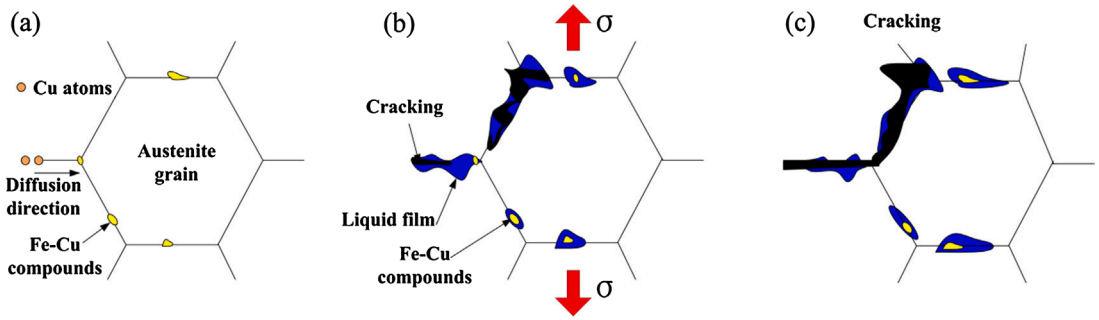

Fig. 12. Liquation cracking model (a) incubation (b) initiation (c) growth [57].

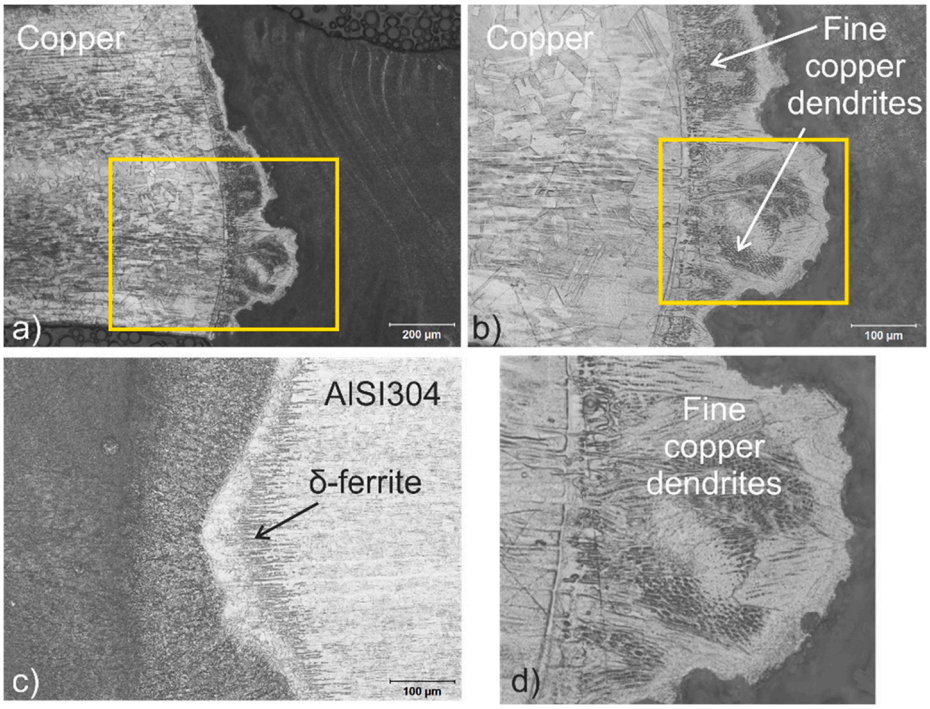

Fig. 14. a) Cu-HAZ and weld interface, b) higher magnification of copper-weld metal interface, c) weld metal-AISI 304 interface, d) fine copper dendrites at higher magnification [64].

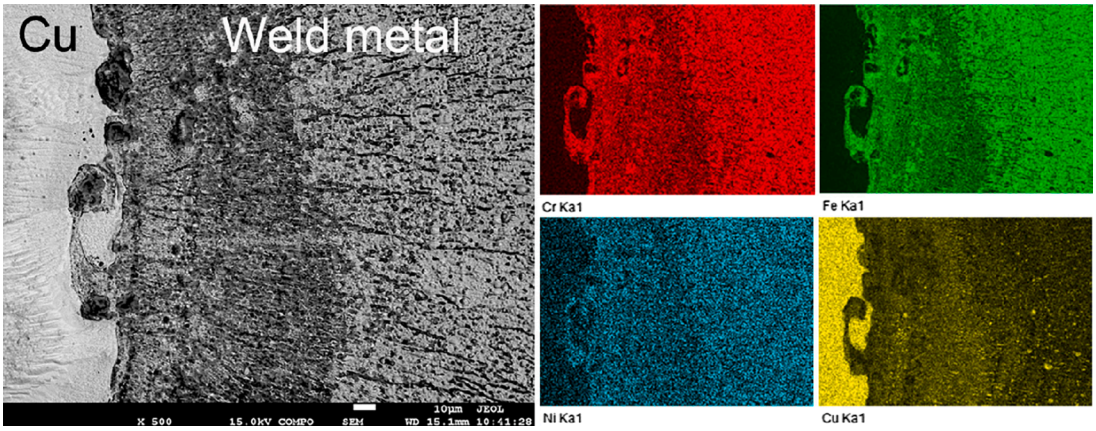

Fig. 15. Distribution of elements across the copper-weld metal interface [64].

intermetallic layer was reduced to below 10 μm. At the same time, the generation of blowholes or voids was mitigated and a deeper penetration was achieved. Moreover, pulse wave created a root-shaped structure which enhanced the weld strength (Fig. 21). Shear strength of 128 MPa was achieved for the dual-beam compared to 71 MPa for single-beam laser-welded samples. Yan et al. [83] tried to improve the microstructure and performance of steel/aluminum welds by using an external magnetic field. The XRD results of the phases formed at the weld zone are presented in Fig. 22. It indicates the presence of Al-rich Fe_2Al_5, $FeAl_3$, $Al_{192.4}Fe_{46.22}$, and a limited amount of Fe-rich FeAl, and Fe_3Al. Adding a magnetic field could alter the content of Fe-rich intermetallics increasing joint strength and reduce susceptibility to hot cracking.

Reduction of joint strength due to corrosion is a well-known issue for Al/steel weld couple [84]. Corrosion resistance of AA6016 and hot-dip galvanized steel (DX56D+Z) laser joint was studied by Wloka et al. [85]. They used an accelerated corrosion test in a salt spray and microelectrochemical measurements. Both tests showed the joining region as the most susceptible to corrosion. The degree of deterioration depended on the cathodic behavior of the adjacent metal. The presence of Fe-containing intermetallics enhanced the corrosion attack due to the strong cathodic behavior. Takehisa et al. [86] investigated the galvanic corrosion of mild steel and AA1100 laser-welded joints by immersion tests in air, distilled water, and salt water. It was revealed that the effect of galvanic corrosion was stronger in salt water than in distilled water.

A relatively novel approach in welding aluminum with steel is using different coatings and interlayers to tailor the intermetallic formation for improved mechanical properties. It has been found that transition metal elements like Mn, Zr, Sn, Ni, and Zn have an inhibitory effect on Fe-Al metallurgical reactions. For example, Jia et al. [87] maintained that the presence of zinc in galvanized steel during laser welding/brazing created $Fe_2Al_5Zn_{0.4}$, a ductile and tough phase. First, $Fe_2Al_5Zn_{0.4}$ forms from Al-rich intermetallics Fe_2Al_5 and $FeAl_3$, and then zinc atoms diffuse into Fe-Al phases substituting Fe atoms. Chen et al. [88] studied the effect of a Ni-foil interlayer during laser welding of A5052 with 201 stainless steel. The weld micrographs, with and without Ni-foil, are shown in Fig. 23a and b, respectively. The interfacial

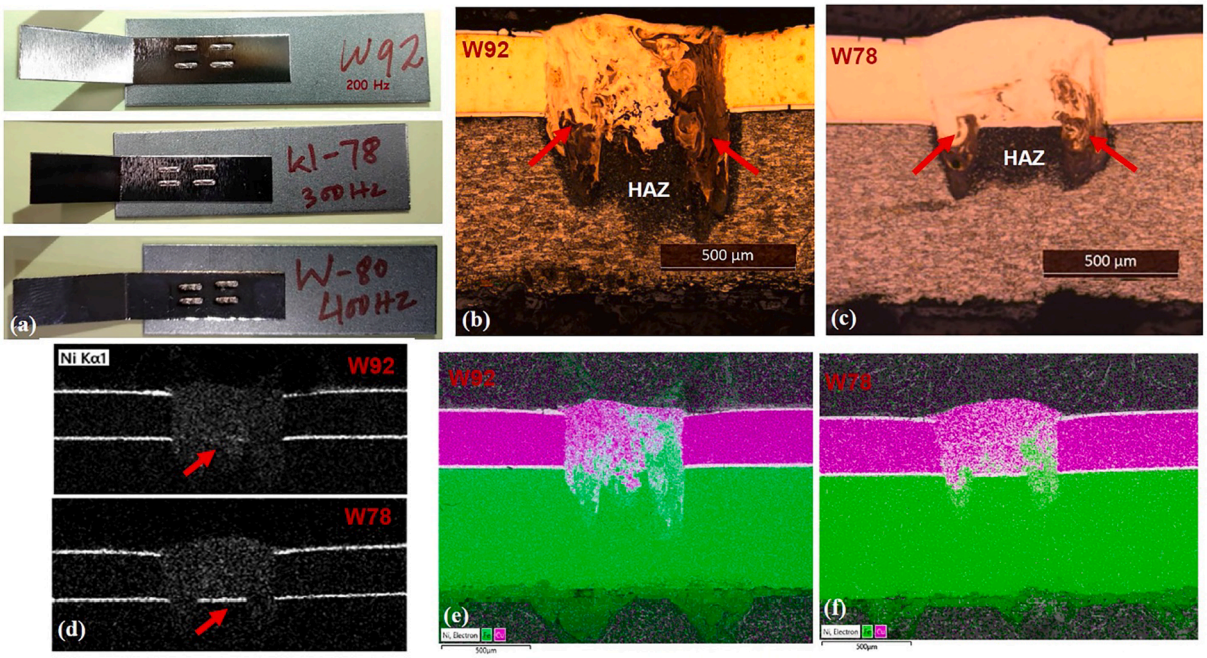

Fig. 16. (a) Weld samples with different wobble frequencies of 200 Hz, 300 Hz, and 400 Hz (b,c) optical microscopy of 200 Hz and 300 Hz samples (d) EDS image showing Ni coating at the weld interface (e,f) elemental distribution in the weld zone [68].

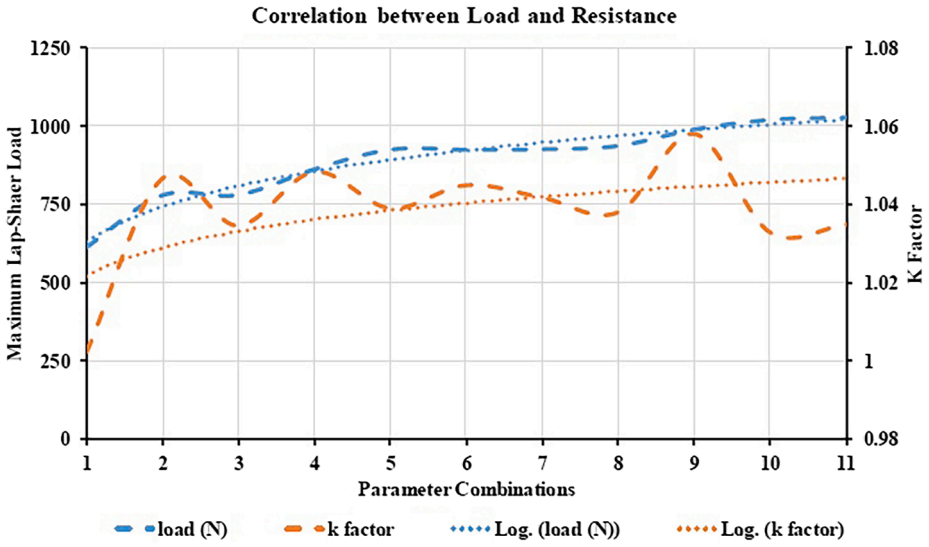

Fig. 17. The correlation between joint resistance and shear strength [69].

microstructure of the sample with Ni interlayer is shown in Fig. 23c, and the corresponding XRD pattern in Fig. 23d. The presence of an intermetallic layer with a thickness of around 20 µm, between the fusion zone and aluminum, is quite visible. This intermetallic layer could be divided into two distinct layers of $FeAl_3$ and $Al_{0.9}Ni_{1.1}$ (dotted line in Fig. 23c). This was an indication that the Ni-foil altered the composition of intermetallics. Other elements such as Cr and Mn were present in intermetallics as solute elements which might have generated a positive effect. Some particles of Fe solid solution (zone E) were detected in the reaction layer but did not change the intermetallics owing to the suppression of diffusion during the high-speed heating/cooling cycle of laser welding. The authors maintained that intermetallics were not observed inside the fusion zone as aluminum mixed into molten steel as a solute element owing to Al having a certain level of solubility in α-Fe. The penetration depth into aluminum had a significant effect on the mechanical properties of the welds. Initially, the tensile strength increased with the weld penetration up to 300 µm, however it then started to decrease with further increase in penetration depth due to the formation of more brittle intermetallics with a higher percentage of Al. Furthermore, tensile testing and microhardness measurements of weld samples revealed that the Ni foil improved the tensile strength while reducing the microhardness of the intermetallic layer. The tensile strength and microhardness measurements are shown in Fig. 24a and b, respectively. In another study, Chen et al. [46] investigated the effect of Cu interlayer on dissimilar laser welding of Q235 low carbon steel and 5052 Al alloy. The Fe-Al interface mainly consisted of α-Al and Al_2Cu eutectic structure, FeAl, $FeAl_2$, a certain amount of Al-Cu intermetallics, Fe_2Al_5, and $FeAl_3$. The Al-Cu interface, on the hand, was mainly composed of the eutectic phase Al_2Cu and the metastable phase of Al-Cu intermetallics. They concluded that the addition of Cu interlayer might

Table 2
Summary of research conducted on laser beam welding of steel and copper.

Materials	Laser process	Joint type	Optimum laser parameters	Weld characteristics	Max. average tensile strength	Electrical resistance	Ref. (year)
1 mm medium-carbon tool steel/ 1 mm copper	Nd:YAG (Pulse mode)	Butt joint	Beam offset: 0.2 mm towards steel Power: 3.2 kW Speed: 0.2 m/min Pulse frequency: 30 Hz Pulse width: 5 ms	No metallurgical bond between Cu and weld metal - Extensive porosity at the joint interface	Not reported	Not reported	[45] (2004)
4.2 mm 316 stainless steel/4.2 mm copper	Nd:YAG (Pulse mode)	Butt joint	Beam offset: 0.4 mm towards Cu Beam focus: 0.1 mm above the surface Power: 4.8 kW	Hot crack clusters along the austenite grain boundaries in stainless steel- HAZ	312 MPa	Not reported	[63] (2004)
10 mm low-carbon Steel (E235A)/10 mm T1 copper	CO_2	Butt joint	Scarf geometry Bram offset: 1 mm towards steel Power: 11 kW Focus: 4 mm Beam diameter: 0.7 mm	A complete metallurgical bond between steel and Cu - Presence of intermixing zone between Cu and weld metal	233.4 N/mm^2	Not reported	[55] (2009)
1.2 mm stainless steel/ 1.2 mm copper	Nd:YAG (Pulse mode)	Butt joint	Power: 3 kW Bram offset: 100 μm towards copper	No cracks in the weld area	Not reported	Not reported	[65] (2010)
2 mm 201 stainless steel/2 mm T2 copper	CO_2	Butt joint	Beam offset: towards Fe Power: 4 kW Beam focus: above the surface	Liquid separation in the weld zone - Rough interfacial morphology between fusion zone and copper - Grain growth in Cu-HAZ	Not reported	Not reported	[53] (2013)
0.25 mm Ni-plated DC04 steel/0.2 mm $CuSn_6$	Fiber	Lap joint	Power: 170 W Speed: 100 mm/s Amplitude: 0.15 mm	Exceptionally large electrical resistances in the weak welds	~ 500 N	Between 0.3 mΩ and 0.6 mΩ	[67] (2014)
2 mm 201 stainless steel/2 mm T2 copper	CO_2	Butt joint	Beam offset: 0.1 mm towards Fe Power: 2 kW Beam focus: above the surface Speed: 1.5 m/min Oblique angle: 2°	Liquid separation in the weld zone - Rough interfacial morphology between fusion zone and copper - Grain growth in Cu-HAZ	260 MPa	Not reported	[56] (2015)
3 mm 304 stainless steel/3 mm copper	CO_2	Butt joint	Beam offset: 50 μm towards Fe Power: 3.5 kW Beam focus: at the surface	More curved weld wall on the steel side and straighter (vertical) on the copper side -Narrower HAZ in stainless steel side	201 MPa	Not reported	[60] (2016)
3 mm 321 stainless steel/3 mm copper	Fiber	Butt joint	No beam offset stainless steel lead-in plate Power: 2.5 kW Speed: 0.6 m/min Beam focus: 12 mm above the surface	No defects such as pores and cracks - Grain growth in Cu-HAZ - Intermediate layer between copper and steel	270 MPa	0.01 Ω	[58] (2017)
0.3 mm Ni-plated steel/Ni-plated Copper	Infrared	Lap joint (Cu on top)	Power: 60 W Frequency: 50 Hz Wobble amplitude: 0.4 mm Wobble frequency: 400 Hz Beam focus: above the surface Speed: 0.5 m/min Pulse on time: 2 ms	Maximum interface width of 462 μm	1.02 kN	Higher electrical resistivity with more mixing of Cu and Fe	[69] (2019)
3 mm 304L stainless steel/3 mm copper	Fiber	Butt joint	No beam offset Power: 1 kW Frequency: 20 Hz Beam diameter: 2.25 mm Speed: 0.3 m/min	A Jagged interface between Cu and weld metal - Primary and secondary liquid separation	224 MPa	Not reported	[66] (2019)
2 mm 304 stainless steel/2 mm copper C21000	CO_2	Butt joint	Beam offset: 0.2 mm towards steel Power: 4 kW Frequency: 20 Hz	A negligible amount of Cu in the fusion zone	236 Mpa	Not reported	[62] (2020)

(*continued on next page*)

Table 2 (*continued*)

Materials	Laser process	Joint type	Optimum laser parameters	Weld characteristics	Max. average tensile strength	Electrical resistance	Ref. (year)
			Speed: 1.5 m/min				
2 mm 304 stainless steel/2 mm T2 copper	Fiber	Butt joint	No beam offset Power: 3 kW Oblique angle: 10° to the side of stainless steel	Polygonal porosity in the wed zone and liquation cracking in stainless steel- HAZ	278 MPa	Not reported	[57] (2020)
1 mm 304 stainless steel/1 mm copper	Nd:YAG (Pulse mode)	Butt joint	Power: 3.5 kW Beam offset: 50 μm towards stainless steel Beam focus: at the surface Pulse duration: 6 ms Pulse energy: 21 J Beam diameter: 0.2 mm Frequency: 10 Hz	Full penetration - the presence of centerline crack - Spatters on the top surface of the weld at the Cu side	146 Mpa	Not reported	[59] (2020)
1 mm 304 stainless steel/1 mm C12200 copper	Disk	Butt joint	Beam offset: 100 μm towards Cu Power: 1.3 kW Speed: 1.8 m/min	Elemental intermixing and metallurgical bond	278 MPa	Not reported	[64] (2020)
1.5 mm 304 stainless steel/1.5 mm copper	Nd:YAG (Pulse mode)	Butt joint	No beam offset Power: 2.5 kW Speed: 0.36 m/min Pulse frequency: 20 Hz	Vermicular dendrite and dendrite layer of austenite in the fusion zone	Not reported	Not reported	[61] (2020)
0.7 mm mild steel DC01/0.3 mm Ni-coated copper C110	Fiber	Lap joint (Cu on top)	Pulse frequency:10 Hz Beam focus: 3 mm above the surface Speed: 100 mm/s Wobble amplitude: 0.6 mm	Cu-Fe composite structure in the weld nugget	660 N	Not reported	[68] (2021)

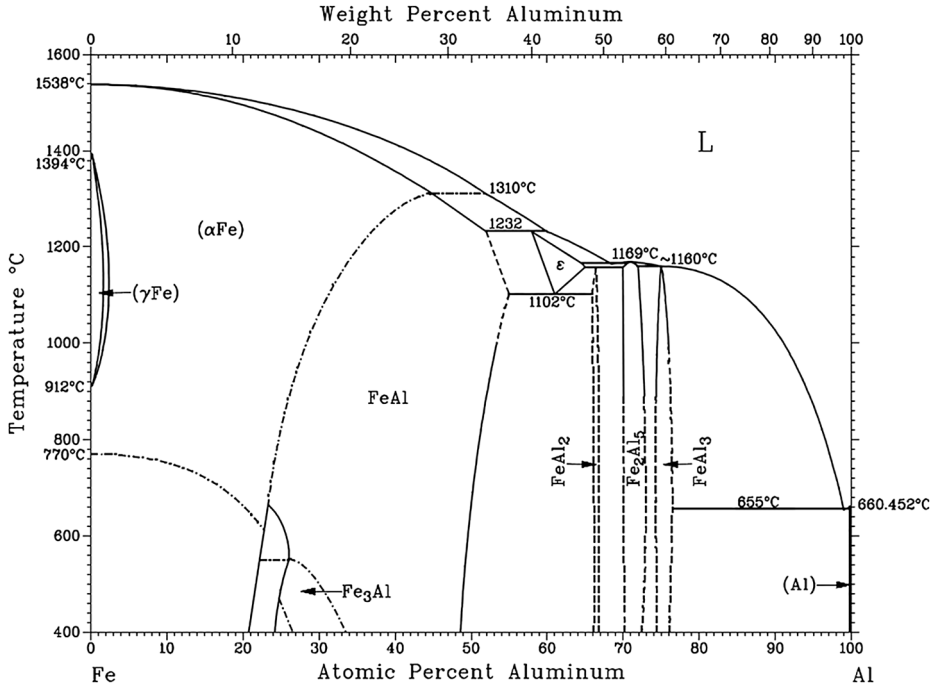

Fig. 18. Equilibrium phase diagram of Fe-Al system [72].

improve the metallurgical reaction but the creation of Al_2Cu intermetalic may have a detrimental effect on the mechanical property that needs further study. They also compared the effect of single beam and dual beam lasers. It was observed that with dual-beam laser better process stability and greater weld width could be achieved leading to higher tensile strength.

Zhou et al. [89] compared the use of Pb and Cu interlayer in laser welding of DC5D+ZF galvanized steel and 6016 Al alloy. Both Cu and Pb interlayer enhanced the tensile strength and elongation of joints. However, Pb was better than the Cu interlayer and resulted in a joint with a

Table 3
Intermetallic compounds in Fe-Al system [73].

Phase	Al content (at.%)	Structure	Microhardness (HV)	Density (g/cm^3)
Fe_3Al	25	Ordered BCC	250–350	6.67
FeAl	50	Ordered BCC	400–520	5.37
Fe_2Al_7	63	Complex BCC	650–680	NA
$FeAl_2$	66–67	Complex rhombohedral	1000–1050	4.36
Fe_2Al_5	69.7–73.2	BCC orthorhombic	1000–1100	4.11
$FeAl_3$	74–76	Highly complex monoclinic BCC	820–980	3.95

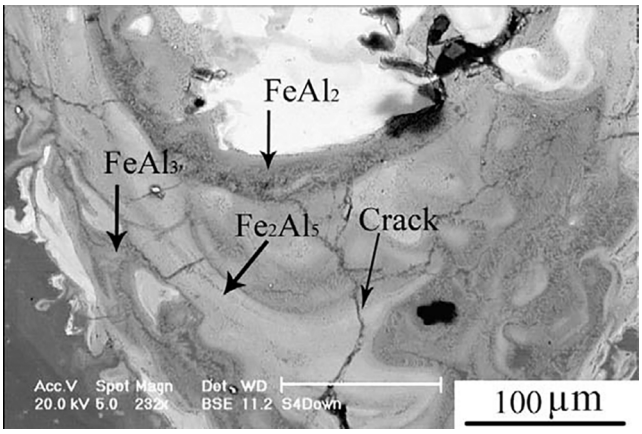

Fig. 19. Micrograph of joint microstructure. Intermetallics are seen at the bottom of the weld near the weld/Al interface [70].

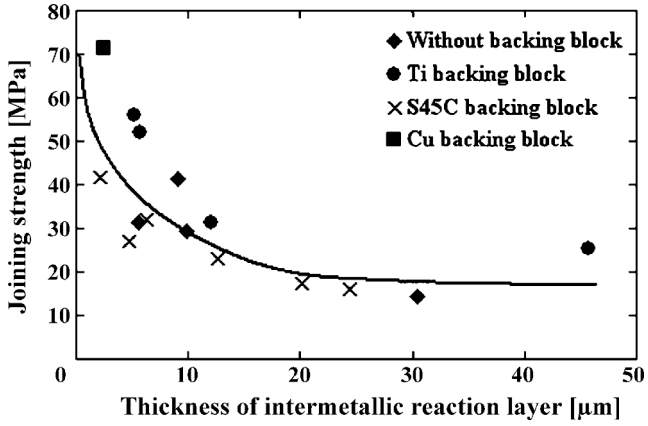

Fig. 20. The relationship between intermetallic layer thickness and joining strength using Ti, S45C, and Cu backing blocks [80].

tensile strength of 73.51 MPa and elongation of 2.37% compared to 49.44 MPa and 1.3% for Cu. In the case of the Pb interlayer, Mg_2Pb was formed at the steel/Al interface, and since it was more stable than FeAl the mechanical properties significantly improved. In another study, Zhou et al. [90] compared the implementation of Mn, Zr, and Sn powders. Fig. 25 illustrates the shear strength of joints with and without powder addition. As can be seen, the best result belonged to Sn (62.17 MPa) owing to the formation of the FeSn phase which similar to Mg_2Pb was more stable than FeAl. Yang et al. [91] compared pure Al, Al-Si, and Zn-Al interlayers. Si was successful in suppressing the growth of the reaction layer. With the reduced reaction layer the fracture load improved. While with the Zn-Al filler metal the thickness of the reaction layer increased to 38 µm the lower microhardness compared to pure Al

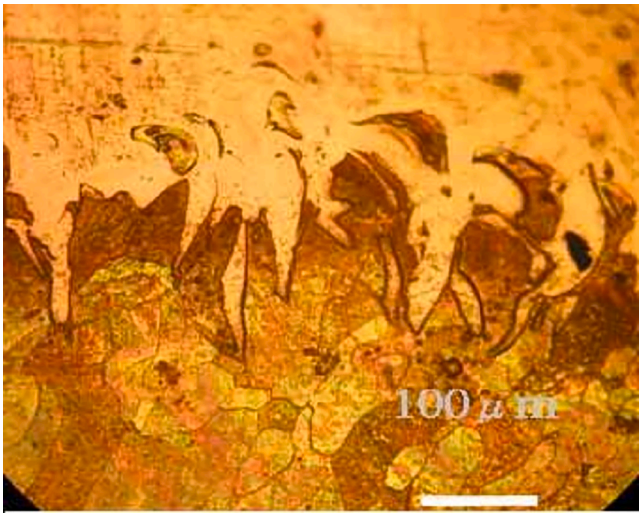

Fig. 21. Root-shape structure at the weld interface [82].

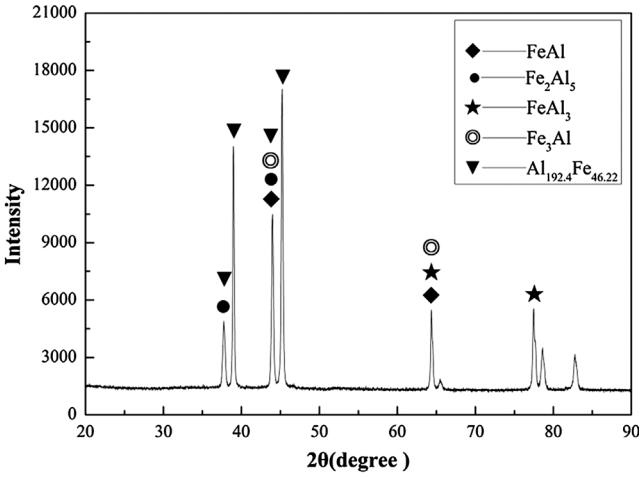

Fig. 22. XRD of intermetallics formed in laser-welded dual-phase steel and Al 6061 [83].

improved the fracture load.

Sun et al. [92] claimed that laser welding/brazing of AA6013 and Q235 low carbon steel was possible in butt configuration using Al-based ER4043 filler metal. However, due to the formation of brittle Fe_2Al_5 and $FeAl_3$ phases, only a joint strength of 120 MPa was achieved. Sierra et al. [93] used the Al-12Si filler wire in laser welding/brazing of AA6016 with low carbon steel (DC04) to investigate the effect of Si on the growth kinetics of Fe-Al intermetallics. Low-thickness (<2 µm) Fe-Al-Si intermetallics with promising mechanical properties were formed at the weld/steel interface. Yang et al. [94] declared the presence of two distinct intermetallics, τ_5-$Al_{7.2}Fe_{1.8}Si$ and θ-$Fe(Al,Si)_3$ at the weld/steel interface in laser welding/brazing of Zn-coated DP980 steel and AA5754-O with a low laser power. The presence of these intermetallics can be seen in Fig. 26. It was observed that due to low heat input the wettability of filler metal was poor. At high laser power, microcracks along with a new planar intermetallic (η-$Fe_2(Al,Si)_5$) were detected owing to a longer time for Fe atoms to diffuse and dissolute. The hard and brittle nature of this intermetallic compound reduced the joint strength. The best result was achieved at medium laser power in which only θ and τ_5 phases were formed while the wettability was improved resulting in a desirable failure at Al/fusion zone interface.

Zhang et al. [95] studied the laser welding/brazing of galvanized steel H220YD to AA6016 using an Al-5Si interlayer. They reported the

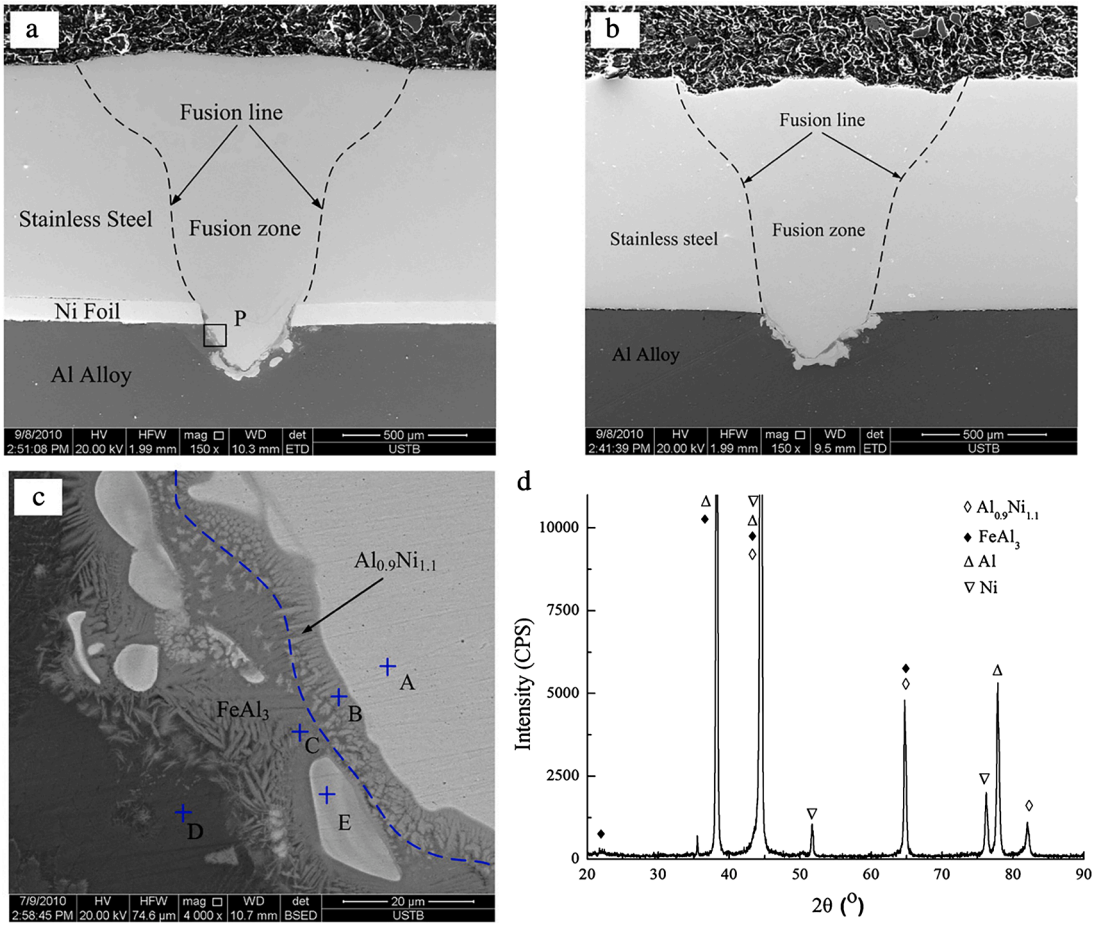

Fig. 23. Microstructure of stainless steel/aluminum joint a) with Ni interlayer, b) without Ni interlayer, c) interfacial microstructure, d) XRD pattern of intermetallics [88].

thickness of intermetallic ranging from 1.3 μm to 13 μm which was composed of α(τ_5)-Al_8Fe_2Si, θ-$Al_{13}Fe_4$, and ζ-Al_2Fe phases. When the thickness of θ-$Al_{13}Fe_4$ and ζ-Al_2Fe was higher than 10 μm, the joint strength was significantly reduced. The effect of Si content on the reaction layer was studied by Xia et al. [96] in laser welded-brazed 6061-T6 Al and DP590 steel using pure Al, Al-5Si, and Al-12Si interlayers. The addition of 5 wt% Si reduced the thickness of η-$Fe_2(Al,Si)_5$ and θ-$Fe(Al,Si)_3$ intermetallic layer owing to the reduction of elemental diffusion area. 12 wt% Si altered the intermetallic components to η-Fe_2Al_5 and τ_5-Al_8Fe_2Si and removed η-$Fe_2(Al,Si)_5$ (Fig. 27). The strength of joints produced with pure Al interlayer was lower than joints with Al-Si filler metal. Moreover, the addition of Si reduced the required laser power during laser welding/brazing process. The highest tensile strength (208 MPa) and ductility were attained with Al-5Si due to proper thickness (3.8–7.5 μm), components (η-$Fe_2(Al,Si)_5$ + θ-$Fe(Al,Si)_3$), and the lower hardness of Si in produced intermetallics. This suggested that η-$Fe_2(Al,Si)_5$ had higher strength and ductility than θ-$Fe(Al,Si)_3$ phase.

Despite significant technological advances and extensive research on laser welding of aluminum to steel during the past four decades, it is still not widely applied mostly owing to insufficient mechanical properties. Progress has been made in optimizing the process parameters, methods, and the use of interlayers. However, controlling the formation and distribution of intermetallic compounds is a major barrier to overcome. Other welds defects such as porosities and cracks need to be addressed as well. Table 4 gives the summary of research carried out on dissimilar laser welding of steel and aluminum alloys.

4. Aluminum-copper

The aluminum and copper welds are of particular interest due to their low weight, cost efficiency, and electrical conductivity similar to that of copper alloys [97]. These joints are commonly used in EV battery pack [10]. The phase diagram of Al-Cu is shown in Fig. 28 [99]. Similar to laser welding of aluminum/steel, brittle intermetallic compounds are formed at the weld interface during aluminum to copper welding, causing crack sensitivity and poor mechanical properties. It has been reported that the intermetallic thickness larger than 5 μm in these welds makes it highly brittle [98]. Properties of the four main intermetallics that can be formed between Al and Cu are presented in Table 5.

Solchencach et al. [101] studied the laser welding/brazing of 500 μm thickness SF-Cu and AA1050 aluminum alloy in an overlap configuration. The laser beam melted the aluminum at the top, which wetted the Cu surface thereby starting the diffusion process. They reported three different seam structures with varied process parameters as shown in Fig. 29. The low energy input led to the formation of voids and the "under-welded" joint. On the other hand, too much energy input melted the copper sheet and created an "over-welded" joint with voids inside solidified aluminum. The formation of aluminum-rich intermetallic (Al_2Cu) with dendritic microstructure was observed near aluminum, while a highly brittle intermetallic (Al_3Cu_4) was present near copper. The effect of intermetallic thickness on the shear strength for different seam welds is shown in Fig. 30. The weld with a homogenous interface structure and an intermetallic interlayer thickness of 3.2 μm had higher strength up to 105 MPa. The "over-welded" seams illustrated better shear strength than "under-welded" ones, potentially due to mechanical interlocking at the over-welded regions. Solchencach et al. [25]

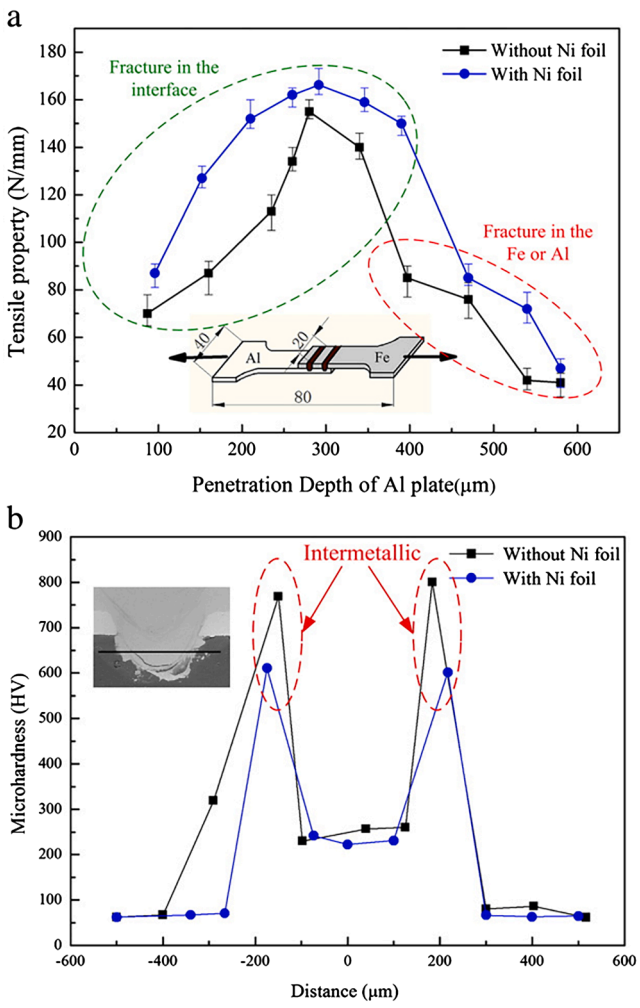

Fig. 24. a) Tensile strength, b) microhardness of the joints between stainless steel and aluminum with and without a Ni interlayer [88].

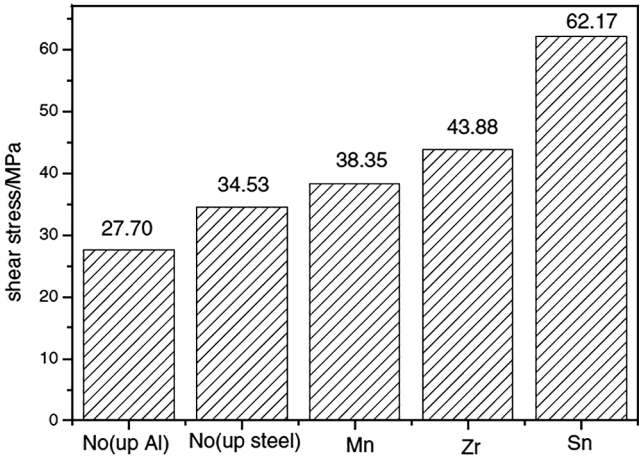

Fig. 25. The average shear strength with and without powder addition [90].

investigated the relationship between shear strength and the electrical resistance in Al-Cu weld joints. They reported an inverse relationship as shown in Fig. 31. Four modulation times of 32 μs, 42 μm, 52 μs, and 62 μs were compared. The lowest electrical resistance was achieved for the welds exhibiting the highest shear strength (32 μs) and containing the intermetallic layer with a thickness of 3.2 μm. An increase in joint

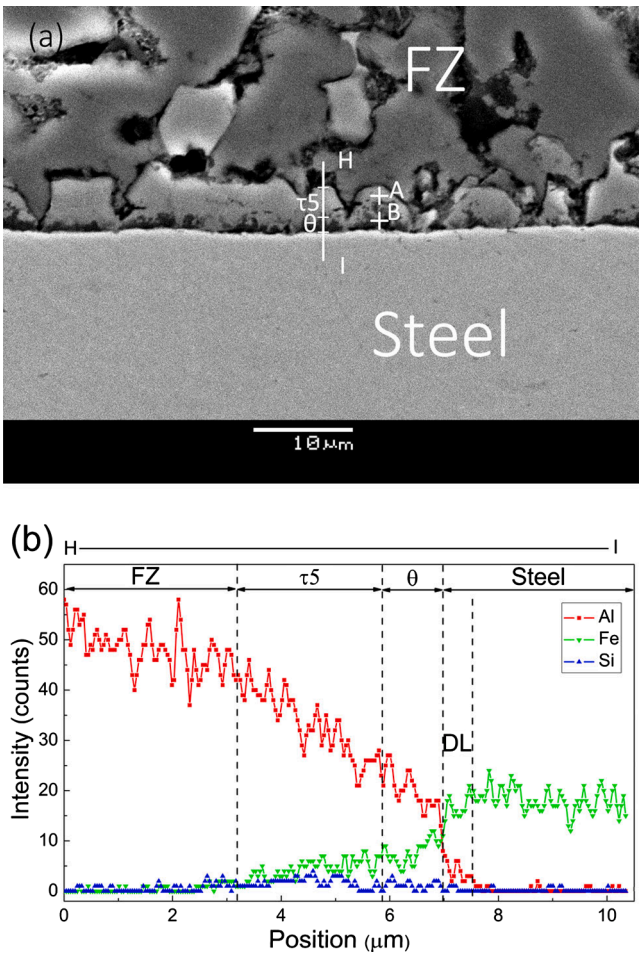

Fig. 26. (a) The interfacial microstructure of Zn-coated DP980 steel and AA5754-O joint at a low laser power (b) EDS line scan [94].

electrical resistance was detected for thicker intermetallic compounds. Similar results have been reported by Braunovic et al. [102] indicating a linear increase in contact resistance with the thickness ofintermetallic compounds.

Lee et al. [99] compared the overlap laser welding of aluminum and copper with aluminum at the top, and when Al was at the bottom. Whenusing aluminum at the top, aluminum was floating on the Cu. However, for aluminum at the bottom, Cu could easily sink into the aluminum. As fluid flow was different for both weld configurations, this influenced the formation of intermetallics. For aluminum at the top, the formation of around 5 μm thickness $AlCu_2$ was observed, close to the interface region. On the other hand, for aluminum at the bottom, a relatively large amount of $CuAl_2$ and Cu_9Al_4 intermetallics were observed. The aluminum and the Cu solid solution were also formed on respective sides for both configurations. The effect of welding speed on the weld quality was also reported. $CuAl_2$, Cu_9Al_4, and CuAl intermetallics were observed inside the weld region for a welding speed of 10 m/min. However, at the higher welding speed of 50 m/min, the formation of intermetallics was suppressed. In addition, the tensile strength improved with increasing the welding speed, reaching 160 MPa for aluminum at the top and 205 MPa for aluminum at the bottom, with the welding speed of 50 m/min. In all samples, the fracture occurred in the intermetallic compound region near the fusion zone interface. The fracture behavior and intermetallic formation in laser-welded samples of copper to aluminum were investigated by Zuo et al. [103]. Fig. 32 shows the weld cross-section micrograph of the sample with a laser power of 1650 W and a welding speed of 95 mm/s. Owing to the higher expansion coefficient of aluminum, an upward convexity of liquid aluminum was

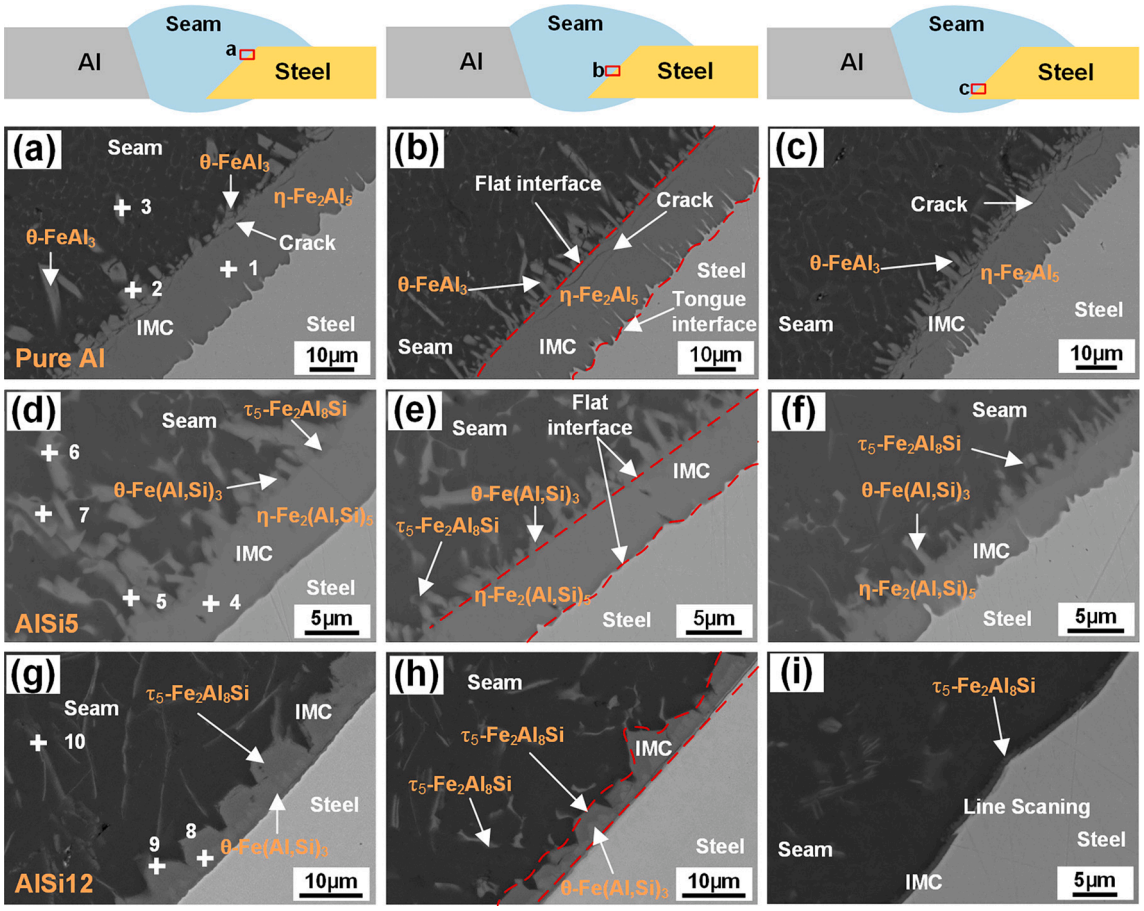

Fig. 27. Microstructure obtained with interlayers (a-c) pure Al (d-f) Al-5Si (g-i) Al-12Si [96].

created during welding. Since there is not sufficient time during solidification for the joint to get back to its original structure, the upward convexity resulted in a shallow weld pool and little mixing of two base metals. The four distinct zones that form the welding interlayer zone between Al and Cu are shown in Fig. 33. Table 6 presents the composition and phase distribution of these zones.

The first zone, adjacent to the Cu consisted of Cu_9Al_4 columnar grains. This was the thinnest and most uniform region. The second zone was a mixture of a net-like eutectic α-Al + θ-$CuAl_2$ (gray area) and θ-$CuAl_2$ (white area) structure. The concentration of $CuAl_2$ was higher on the Cu side and by moving away from the copper, the $CuAl_2$ concentration decreased. Zone 3 contained a eutectic phase similar to zone 2, but finer in size and with an interlamellar spacing of below 1 μm. In zone 4, the growth of the solidification front and the segregation of alloying elements created the dendrite microstructure. It was found that the presence of a thin, continuous, and uniform γ_2-Cu_9Al_4 phase improved the shear strength. In contrast, the brittle θ-$CuAl_2$ phase had a detrimental effect on the weld strength, and the fracture that occurred in this zone illustrated a weaker cohesion in the aluminum side.

The application of sinusoidal beam oscillation was studied by Fetzer et al. [104] in overlap laser welding of oxygen-free copper and high-purity aluminum. They reported that by using suitable oscillation parameters, the weld composition could be managed. In the case of the smaller amplitude of 0.25 mm the weld composition was very inhomogeneous and large cracks were seen. However, the larger amplitude of 0.75 mm decreased the amount of copper in the weld zone.Furthermore, the fused copper was distributed more homogeneously. No cracks were seen in this case. Circular laser beam oscillation was applied by Dimatteo et al. [28] in laser welding of Al and Cu sheets. Low electrical contact resistance and good mechanical properties were achieved with double weld seams. Lerra et al. [105] focused on pulse shape and separation distance in Nd:YAG laser welding of Al and Cu. With the process optimization, a low penetrating depth with a maximum tensile load of over 110 kgf was achieved. They also reported that preheating the sample before welding resulted in better mechanical properties and electrical resistance.

A number of studies have been carried out on the selection of a proper filler alloy to minimize defects and improve mechanical properties in the Al-Cu joint. The effect of a tin interlayer in laser welding of Al 3003-H14 and Cu110 was studied by Hailat et al. [106]. Fig. 34 shows the Al-Cu weld cross-section with and without the tin interlayer. Large porosities can be seen in aluminum in the weld with Sn interlayer. However, the fracture occurred away from these porosities therefore they did not seem to affect the joint strength andwelds with tin filler metal exhibited a better lap shear strength possibly due to the formation of Cu_6Sn_5 and Cu_3Sn. Mys and Schmidt [107] declared that while using a Ni interlayer resulted in only a slight improvement in the tensile strength of Al-Cu joints, Ag and Sn foils considerably improved the tensile strength. The samples welded without the silver interlayer showed a very small recrystallization zone on the copper side following by hard and brittle Cu-Al intermetallics. However, the joint produced with silver exhibited a uniform distribution of Ag atoms in the silver-rich matrix. The high concentration of silver resulted in reasonable ductility and fatigue property. Similar results confirming the influence of using an Ag interlayer on the joint strength have been reported by Esser et al. [108].

The laser beam offset has been recommended to restrict the growth of intermetallics in butt laser welding of aluminum and copper, quite similar to laser welding of steel to Cu. Mai and Spowage [45] investigated the laser welding of Cu and AA4047 aluminum alloy in the butt

Table 4
Summary of research conducted on laser beam welding of steel and aluminum.

Materials	Interlayer	Laser process	Joint type	Optimum laser parameters	Intermetallics	Max. average tensile strength	Ref. (year)
1.2 mm Dual-Ten 590 steel/1.6 mm A6022-O aluminium	–	Not reported	Lap joint (steel on top)	Power: 3 kW Spot radius: 30 mm Pure Cu backing block	Not reported	70 Mpa	[80] (2007)
0.77 mm Zinc-coated low carbon steel/6016 T4 aluminum	–	Nd:YAG	Lap joint (Al on top)	Power: 1.6–2 kW Speed: 2–2.4 m/min Inclination angle: 35° Beam focus: +10 and + 11 mm	$FeAl_3$ - Fe_2Al_5	Above 200 N/mm	[74] (2007)
1.2 mm low carbon steel DC04/1 mm 6016-T4 aluminum	1 mm filler wire 4047 Al alloy (Al-12Si)	Nd:YAG	Lap joint (Al on top)	Power: 2 – 2.5 kW Inclination angle: 30°	Thin (<2 μm) Fe-Al-Si intermetallics	190 N/mm	[93] (2008)
0.8 mm low carbon steel st14/2 mm 5754 aluminum	–	Nd:YAG (Pulse mode)	Lap joint (steel on top)	Peak power: 1.43 kW Pulse duration: 5 ms Overlapping factor: 80%	$FeAl_2$ – $FeAl_3$ - Fe_2Al_5	Not reported	[70] (2010)
0.8 mm JSC270CC steel/1.2 mm A6111-T4 aluminium	–	Nd: YAG (Continuous and pulse mode)	Lap joint (steel on top)	CW laser power: 390 W PW peak power: 2.61 kW Pulse frequency: 5 Hz Pulse width: 2 ms Speed: 0.06 m/min	IMC layer below 10 μm	128 Mpa	[82] (2010)
1 mm 201 Stainless steel/ 1 mm 5052 Al	0.1 mm Ni foil	CO_2	Lap joint (steel on top)	Power: 1 kW-3 kW Speed: 1 m/min – 3 m/min Beam focus: +0.2 mm	$FeAl_3$ and $Al_{0.9}Ni_{1.1}$	~ 160 N/mm	[88] (2012)
1.2 mm H220YD galvanized steel/ 1.15 mm 6016 aluminum	1.2 mm filler wire 4043 Al alloy (Al-5Si)	Fiber	Butt joint	Power: 2.3 kW – 2.6 kW Speed: 1 m/min Filler wire feeding speed: 2.22 m/min Beam focus: +5 mm	1.3 μm to 13 μm composed of α(τ_5)-Al_8Fe_2Si, θ-$Al_{13}Fe_4$, and ζ-Al_2Fe	162 MPa	[95] (2013)
0.75 mm DP590 galvanized steel/1 mm 6061-T6 aluminum	–	Fiber	Lap joint (Steel on top)	Laser preheating power: 4 kW Laser welding power: 3 kW Speed: 100 mm/s	iron-rich IMCs (Fe_3Al, FeAl) and the Al-rich IMCs ($FeAl_2$, Fe_2Al_5)	~ 160 N/mm	[79] (2014)
1 mm DC04 steel/1 mm 6111-T4 aluminium	–	Fiber	Lap joint (steel on top)	Cu backing bar Power density: 2.75 E-3 MW/cm^2 Interaction time: 3 s Specific point energy: 10.95 kJ Standard deviation: 1.26 μm	$FeAl_3$ - Fe_2Al_5	130 MPa	[81] (2014)
0.8 mm hot-dip galvanized steel/ 1.5 mm A5052-H34 aluminum	70–110 μm diameter pure Al powder	Nd:YAG	Lap joint (Al on top)	Laser power: 2250 W Defocusing distance: 12 mm Welding speed: 1 m/min Beam incline: 30°	$FeAl_3$ - Fe_2Al_5 $Fe_2Al_5Zn_{0.4}$	Not reported	[87] (2015)
2.5 mm Q235 low-carbon steel/2.5 mm 6013 aluminium	1.2 mm Al alloy (ER4043)	Fiber	Butt joint	Laser power: 3.05 kW Welding speed: 1.8 m/min Beam angle: 12° Beam focus: 2 mm above the surface	$FeAl_3$ - Fe_2Al_5 – Al-Si eutectic	120 MPa	[92] (2015)
1 mm hot-dip 980 DP galvanized steel/2 mm 5754-O Al	1.6 mm filler wire 4047 Al alloy (Al-12Si)	Diode	Lap joint (Al on top)	Laser power: 2 kW Welding speed: 1 m/min Beam focus: 0 mm	θ-$Fe(Al,Si)_3$ and τ_5-$Al_{7.2}$ $Fe_{1.8}Si$	~ 215 N/mm	[94] (2015)
1.2 mm DC56D + ZF steel/1.15 mm 6016 aluminium	0.02 mm pure Cu or Pb foil	CO_2	Lap joint (steel on top)	Laser power: 1600 W Welding speed: 1100 mm/min Beam focus: −0.5 ± 1.0 mm	$Al_{0.4}Fe_{0.6}$, Mg_2Zn_{11} Mg_2Pb	73.51 MPa	[89] (2016)
1 mm low carbon steel Q235/1 mm 5052 aluminum	0.1 mm Cu foil	CO_2	Lap joint (steel on top)	Laser power: 2.5 kW dual-beam 1.6 kW single-beam Welding speed: 0.9–1.25 m/min dual-	The Fe-Al interface: α-Al and Al_2Cu eutectic structure, FeAl, $FeAl_2$, a certain amount of Al-Cu intermetallics, Fe_2Al_5, and $FeAl_3$. The Al-Cu interface: the eutectic phase Al_2Cu and metastable phase of Al-Cu intermetallics.	74 N/mm dual-phase 65 N/mm single-phase	[46] (2016)

(*continued on next page*)

Table 4 (*continued*)

Materials	Interlayer	Laser process	Joint type	Optimum laser parameters	Intermetallics	Max. average tensile strength	Ref. (year)
				beam and 1.5–1.75 m/min single-beam			
0.8 mm 316L stainless steel/0.8 mm 1060 pure aluminum	–	Nd:YAG (Pulse mode)	Lap joint (steel on top)	Laser mean power: 285 W Welding speed: 4 mm/s Beam focus: −0.6 mm	Fe- rich IMCs	46.2 ± 1.9 N/mm	[76] (2016)
1.4 mm DC56D + ZF steel/1.2 mm 6016 aluminium	75 μm pure Mn, Zr, or Sn powder	Fiber	Lap joint (steel on top)	Welding power: 1800–2000 W Welding speed: 45–50 mm/s Focus beam: +2 mm	FeAl, FeSn, $FeAl_3$	62.17 MPa	[90] (2016)
2.5 mm DP600 steel/3 mm 6061 aluminium	–	Fiber-coupled diode	Lap joint (steel on top)	Laser power: 4 kW Scanning speed: 5 mm/s Pulse duration: 10 ms	$FeAl_3$ - Fe_2Al_5	Not reported	[75] (2018)
1.2 mm DP590 dual-phase steel/1.5 mm 6061-T6 aluminium	1.6 pure Al-1100, $AlSi_5$-4043, and $AlSi_{12}$-4047	Fiber	Butt joint	Laser power: 2 kW Welding speed: 0.5 m/min Laser offset: 0.4 mm towards Al Focus distance: +20 mm	τ_5- Fe_2Al_8Si, θ-$Fe(Al,Si)_3$	208 MPa	[96] (2018)
1 mm DP980 steel/1.5 mm 5754 aluminium	1.6 mm Al-1100, $AlSi_{12}$, $ZnAl_{22}$	Diode	Lap joint (steel on top)	Laser power: 1.0–2.8 kW Welding speed: 0.2–1.0 m/min Laser offset: 0 mm Focus distance: 0 mm	Si interlayer: $Al_{7.2}$ $Fe_{1.8}Si$ and $Fe(Al,Si)_3$ Zn-Al interlayer: $Fe_2Al_{5-x}Zn_x$, $FeZn_{10}$, and a small amount of Al-rich amorphous phase	1233 N	[91] (2018)
1.3 mm press-hardened steel/2 mm 5052 aluminum	0.05 mm and 0.1 mm brass	Fiber	Butt joint	Laser power: 1.2 kW Laser offset: 0.2 mm towards steel Welding speed: 12 mm/s	Fe_3Al - Fe_2Al_5 - FeAl	56.4 MPa	[71] (2019)
1 mm low carbon DC04/1 mm 6016 aluminum	–	Fiber	Lap joint (steel on top)	Laser power: 1400 W Welding speed: 40 mm/s Beam focus: 0 mm	$FeAl_3$ - Fe_2Al_5	Not reported	[78] (2019)
1 mm DP1000 steel/1 mm 1050 aluminium	–	Nd:YAG (Pulse mode)	Lap joint (steel on top)	Laser power: 6.48 kW Pulse duration: 14 ms	Not reported	120 MPa	[77] (2019)
1 mm DP590 galvanized steel/1 mm 6061-T6 aluminum	–	Fiber	Lap joint (steel on top)	Laser power: 3 kW Welding speed: 5 m/min Focus distance: +2 mm	Fe_2Al_5, $FeAl_3$, $Al_{192.4}Fe_{46.22}$ phase and a limited amount of FeAl and Fe_3Al	1.22 kN	[83] (2019)

configuration. The laser beam offset of 0.2 mm towards aluminum produced crack-free welds with an elemental concentration of 48.4% Al, 24.3% Si, and 27.2% Cu. The weld nugget had a very high hardness compared to the parent materials that was attributed to the supersaturated solid solution or the formation of GP-zones. However, the increase in welding speed to more than 100 mm/min led to the solidification cracking at the weld joint. $AlSi_{12}$ was used as filler materials for laser welding of pure aluminum and copper by Weigl and Schmidt [109]. Both $AlSi_{12}$ and $CuSi_3$ intermetallics enhanced the ductility of the joints and reduced the absolute value and fluctuation of microhardness. However, the best results were achieved with $AlSi_{12}$ owing to its higher percentage of Si. It reduced the viscosity and enhanced the turbulence of the molten metal thereby improving the elemental mixture in the weld zone.

Similar to laser welding of steel and aluminum optimization of the welding process parameters, and the use of interlayers has been the subject of several investigations. The application of beam oscillation has been explored as well. Despite these improvements, the effect of potential interlayers on the formation of new intermetallics needs further studies. The optimization of process parameters should be further studied too. Table 7 gives a summary of the research conducted on dissimilar laser welding of aluminum and copper thus far.

5. Steel-nickel

Steel-nickel dissimilar joint is another potential combination in EV battery pack especially between tab and case of cylindrical cells. Hu et al. [110] developed a three-dimensional transient numerical model for heat and mass transfer to calculate weld geometry and elemental distribution in laser spot welding of 304 stainless steel and nickel. They observed that elements were uniformly distributed in the weld pool which agreed well with calculated results. Porosity formation in laser welding of pure nickel and martensitic stainless steel was studied by Zhang et al. [111]. They concluded that shielding gas had no effect on the porosity formation, but there was a direct relationship between the pulse width and the number of porosites. When the pulse width was below 5 ms the porosity formation was completely suppressed resulting in a better joint in terms of mechanical strength. Li et al. [112] investigated the effect of different heat inputs in laser welding of 304 stainless steel and Ni. Near-free joints were achieved indicating applicability of laser welding for joining 304 stainless steel and nickel. It was also observed that the cooling rate was highly dependent on the heat input affecting the grain dimension.

The information regarding the dissimilar laser welding of steel and nickel is very limited and the metallurgical aspects of this joint has not

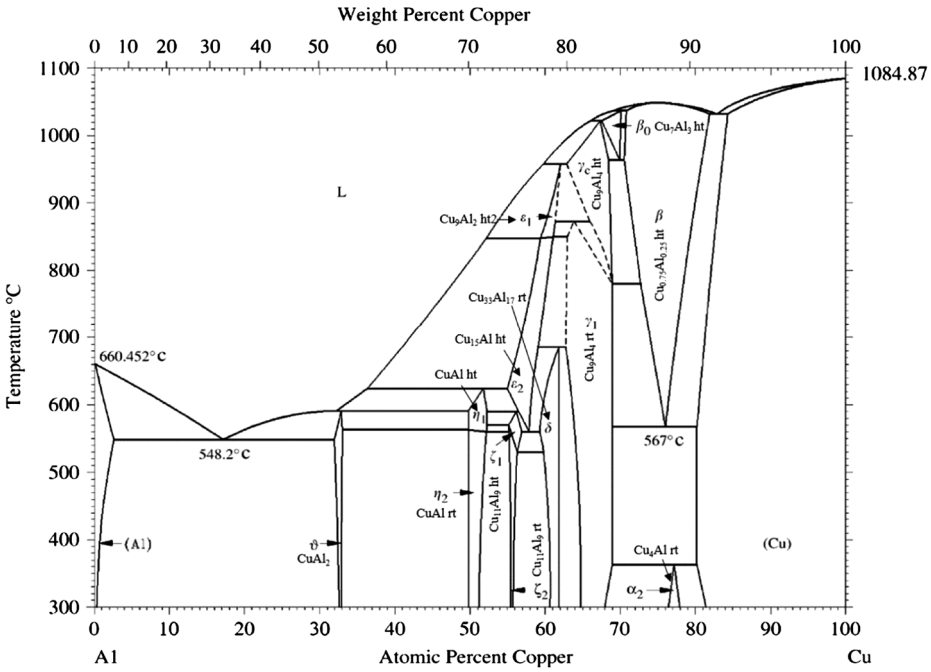

Fig. 28. Equilibrium phase diagram of Al-Cu system [99].

Table 5
Properties of important intermetallics between Al and Cu [100].

Phase	Cu content (at.%)	Structure	Microhardness (HV)	Density (g/cm^3)	Specific resistance (μΩ cm)
$CuAl_2$	33	Body-centered tetragonal	630	4.34	8
CuAl	51	Body-centered orthorhombic	905	5.13	11.4
Cu_4Al_3	55.5	Monoclinic	930	NA	12.2
Cu_9Al_4	66	Body-centered cubic	770	6.43	14.2

been much explored yet. The summary of the research conducted on laser welding of steel and nickel is presented in Table 8.

6. Summary and outlook

Laser welding is a robust and contact-free welding process with high control of energy deposition which provides a crucial way for joining temperature-sensitive and dissimilar material components such as battery cells in the EV battery system. Laser welding of dissimilar materials has continued to develop over the past two decades. However, despite several studies on different laser sources, optimization of process parameters, and various interlayers, metallurgical defects such as incomplete bonding, brittle intermetallic phases, corrosion, excessive porosities, and cracking have persisted. These defects greatly undermine the mechanical and electrical performance of EV battery joints. Thus, further investigation is needed before laser welding can be widely used for EV battery manufacturing.

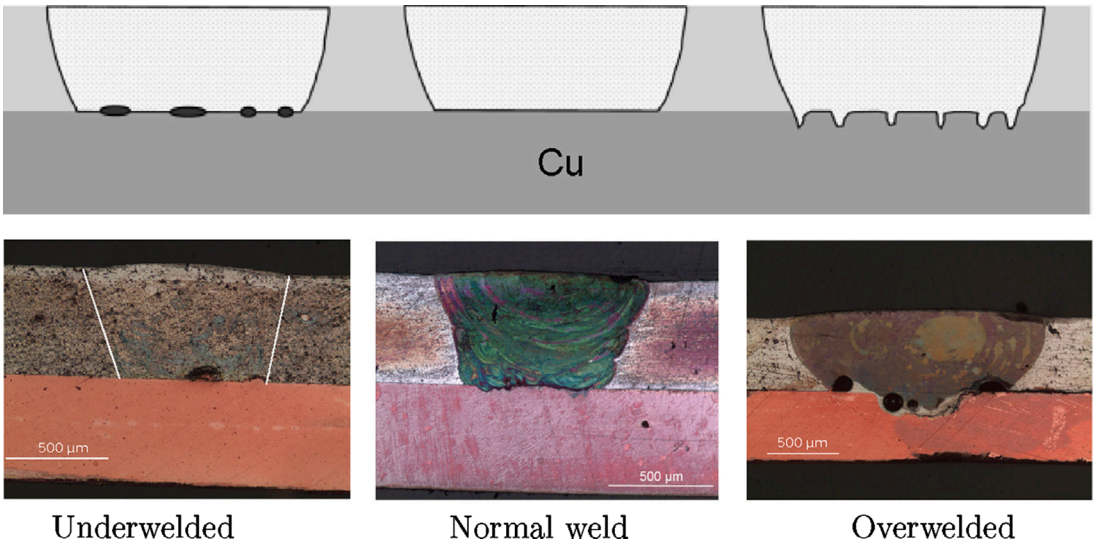

Fig. 29. Three different weld seam structures corresponding with welding conditions [101].

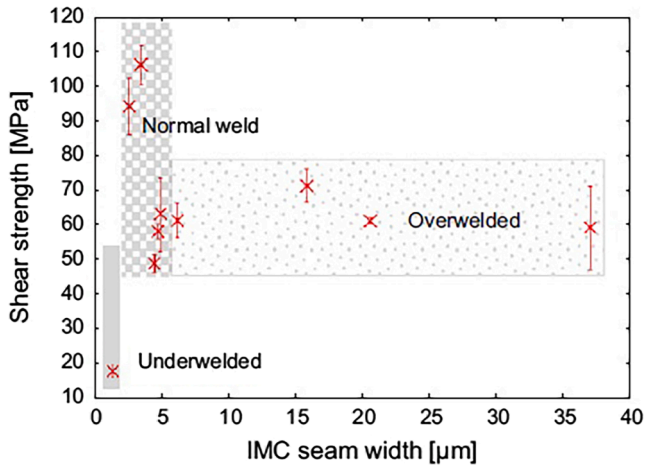

Fig. 30. The correlation between intermetallic layer thickness and shear strength in joints with different welding seams [101].

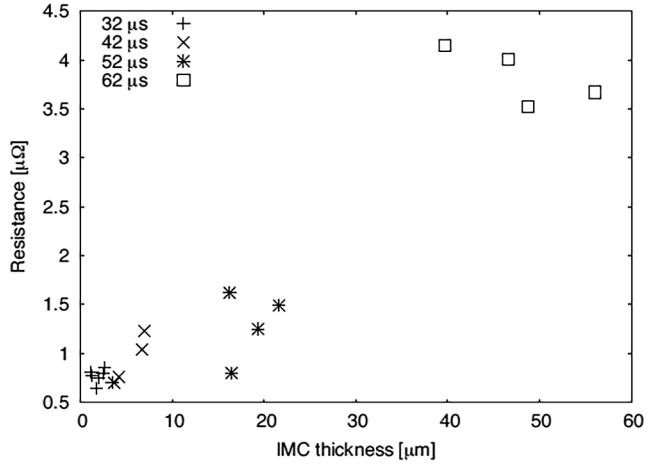

Fig. 31. The correlation between the intermetallic thickness and interface resistance [25].

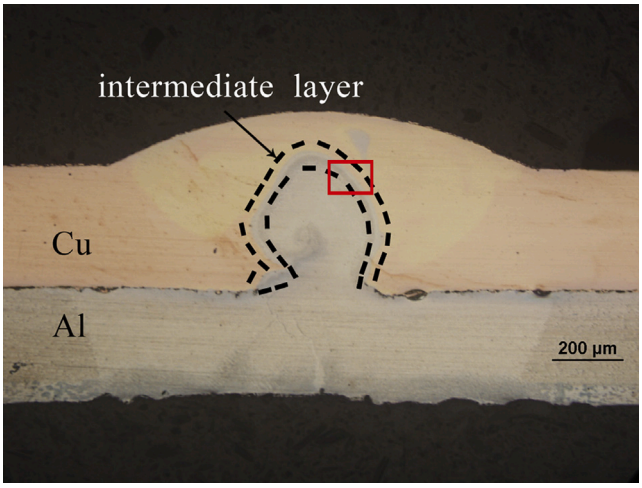

Fig. 32. Micrograph of weld cross-section with a laser power of 1650 W and a welding speed of 95 mm/s [103].

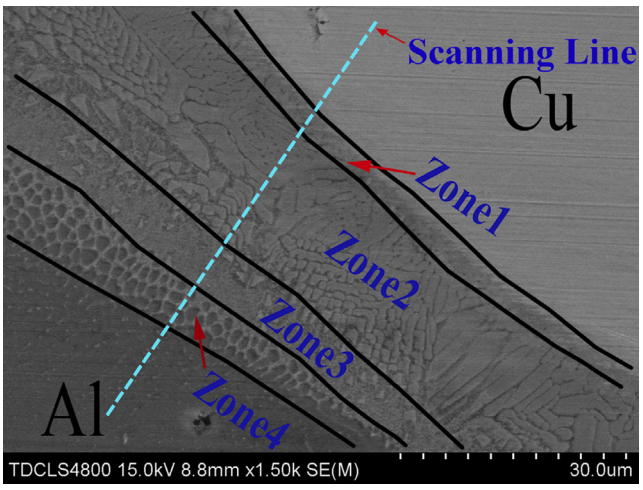

Fig. 33. Morphology of four distinct zones in the intermediate layer between Cu and Al [103].

Table 6
Chemical composition of phases observed in Fig. 33 [103].

Zone	Concentration (wt% Cu)	Phase
1	62.18–64.45	Columnar grain (γ_2-Cu_9Al_4)
2	45.34–51.95 (white) 30.12–41.19 (gray)	Lump (θ-$CuAl_2$) + eutectic (α-Al + θ-$CuAl_2$)
3	30.27–36.61	Eutectic (α + θ)
4	≤8.55	Dendrites (α-Al)

In this review paper, the research on the laser welding process for joining the different combinations of dissimilar materials including steel-copper, steel-aluminum, aluminum-copper, and steel-nickel was summarized. Based on the studies so far, some suggestions for future research in this field are as follows:

(1) The precise control of heat input through the optimization of process parameters can improve the weld quality by controlling the thickness of IMCs and depth of penetration. However, owing to the low thickness and incompatible properties of materials involved in EV battery further investigations are needed to determine the optimum welding parameters such as welding speed and beam oscillation frequency for each weld combination and configuration.
(2) The use of appropriate interlayer materials and coatings can tailor the microscopic structure through modification of IMC composition which can potentially improve mechanical performance and reduce electrical resistivity. The applicaton of potential interlayers especially when there is a higher possibility for intermetallic formation has not been fully explored yet.
(3) Industrial lasers in infrared wavelength (1064 nm) have typically been used thus far for joining dissimilar materials in keyhole mode. Novel lasers with lower wavelengths and higher power including blue laser (wavelength~450 nm) and green laser (wavelength~515 nm) systems have been introduced in recent years with much higher energy absorption on highly reflective materials such as copper and aluminum which are widely used as battery tabs or busbars. However, these laser systems still have not been used for dissimilar welding of battery materials.
(4) There have hardly been any reports on the evolution of intermetallic phases during the battery's long-term service. To guarantee the reliability of dissimilar joints, the effects of various thermal conditions on the intermetallic formation and thickness should be investigated.

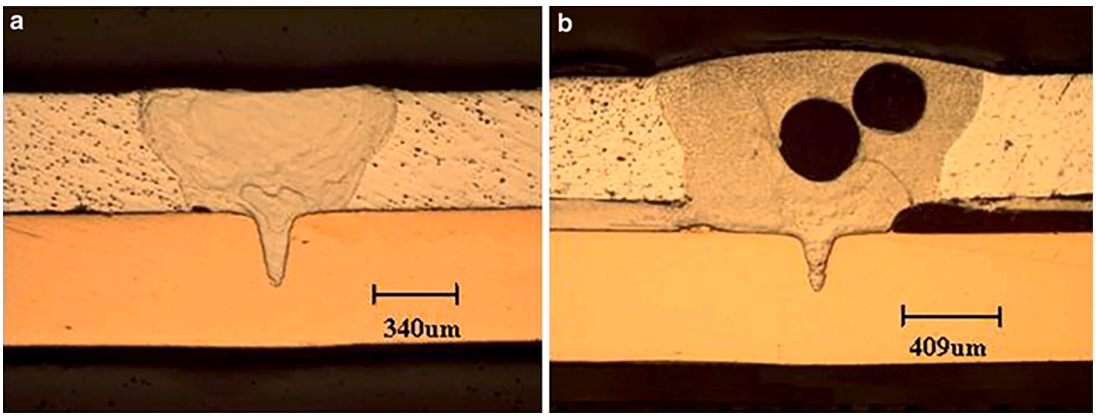

Fig. 34. Al-Cu laser weld (a) without Sn filler metal (b) with Sn filler metal [106].

Table 7
Summary of research conducted on laser beam welding of aluminum and copper.

Materials	Interlayer	Laser process	Joint type	Optimum Laser parameters	Intermetallics	Max. average tensile strength	Ref. (year)
1 mm copper/ 1 mm 4047 Al	–	Nd:YAG (Pulse mode)	Butt joint	Power: 275 W Speed: 75 mm/min Pulse frequency: 15 Hz Pulse width: 8 ms	Not reported	Not reported	[45] (2004)
1.2 mm Cu/1.2 mm Al	0.1 mm Ag 0.1 mm Ni	Nd:YAG (Pulse mode)	Lap joint (Cu on top)	Laser power: 3 kW Beam offset: 0.1 mm towards Al	Not reported	800 N	[108] (2004)
1.2 mm Cu/1.2 mm Al	0.1 mm Ag	Nd:YAG (Pulse mode)	Lap joint (Al on top)	Laser power: 3 kW Beam offset: 0.1–0.2 mm towards Al	Not reported	800 N	[107] (2006)
1 mm Cu/1 mm Al	1.6 mm filler wire $AlSi_{12}$	Pulse mode	Butt joint	Laser power: 200 W	Not reported	Not reported	[109] (2011)
0.54 mm 110-*H*00 copper/0.49 mm 3003-H14	100 μm tin	Fiber	Lap joint (Al on top)	Laser power: 460 W Welding speed: 1 m/min Beam incline: 15°	Not reported	780 N	[106] (2012)
0.5 mm SF-Cu copper/0.5 mm AW1050A	–	Fiber	Lap joint (Al on top)	Laser power: 400 W Beam focus: 1 mm below the surface	Al_2Cu – Al_4Cu_9	121 MPa	[101] (2013)
0.3 mm Copper /0.3 mm Aluminium A1050	–	Fiber	Lap joint	Laser power:1 kW Welding speed: 50 m/min	$CuAl_2$ – Cu_9Al_4 - CuAl	205 Mpa	[99] (2014)
0.3 mm T2 Copper/0.3 mm Aluminum A1060	–	Nd:YAG	Lap joint (Cu on top)	Laser power: 1.65 kW Welding speed: 95 mm/s	$CuAl_2$ – Cu_9Al_4	539.52 N	[103] (2014)
1 mm Cu/1 mm Al	–	Fiber	Lap joint (Al on top)	Laser power: 3.25 kW Feed rate: 6 m/min Beam incline: 10°	Not reported	Not reported	[104] (2016)
0.3 mm C1020-HO Copper/ 0.45 mm Aluminum A1050	2.5 μm electroplated Ni layer on Cu	Fiber	Lap joint (Cu on top)	Laser power: 800 W Welding speed: 134 mm/s Wobbling amplitude: 0.7 mm	Not reported	120 kgf	[28] (2019)
0.3 mm C1020-HO Copper/ 0.45 mm Aluminum A1050	2.5 μm electroplated Ni layer on Cu	Nd:YAG (Pulse mode)	Lap joint (Al on top)	Laser power: 6 kW Pulse energy: 13 J Pulse separation distance: 0.1–0.32 mm	Not reported	110 kgf	[105] (2019)

(5) Most of the studies so far have been conducted on the static mechanical properties of laser-welded dissimilar joints, while hardly any data is available on fatigue behavior despite its importance in predicting the structural performance under cyclic loading.
(6) While there has been limited work on the electrical performance of dissimilar joints in EV battery, the electrical resistivity of joints or "connection resistance" has not been fully explored. The high resistance leads to energy loss and heat generation at the weld interface during the charging and discharging. Therefore, future studies and standardization of measurement methods are needed in the area.
(7) Some progress has been achieved in studying the corrosion performance of laser-welded joints especially about galvanic corrosion of steel/aluminum couple. However, the relationship between corrosion and mechanical properties in laser welding of EV battery materials requires further investigation.

Table 8
Summary of research conducted on laser beam welding of steel and nickel.

Materials	Laser process	Joint type	Optimum laser parameters	Weld characteristics	Ref. (year)
2 mm nickel/ 2 mm 304 stainless steel	Nd: YAG	Butt joint	Laser power: 650 W	Uniform distribution of element Fe in the weld pool	[110] (2012)
0.3 ~ 0.5 mm pure nickel/ stainless steel SUS440C	Fiber	Lap joint (Ni on top)	Welding speed: 4.7 mm/s Beam spot size: 0.1 mm Laser peak power: 300 W	Complete elimination of porosities	[111] (2013)
2 mm nickel/ 2 mm 304 stainless steel	Nd: YAG	Butt joint	Laser power: 800 W Laser speed: 10–30 mm/ s Laser spot: 0.57 mm	Nearly defect-free joints	[112] (2018)

Declaration of Competing Interest

The authors declare that they have no known competing financial interests or personal relationships that could have appeared to influence the work reported in this paper.

References

[1] I. Iea, CO2 emissions from fuel combustion highlights, International Energy Agency Paris. (2012).
[2] H. Hao, Y. Geng, J. Sarkis, Carbon footprint of global passenger cars: Scenarios through 2050, Energy 101 (2016) 121–131.
[3] S.M.S.U. Eskander, S. Fankhauser, Reduction in greenhouse gas emissions from national climate legislation, Nat. Clim. Change 10 (8) (2020) 750–756.
[4] R.W. Wimbadi, R. Djalante, From decarbonization to low carbon development and transition: A systematic literature review of the conceptualization of moving toward net-zero carbon dioxide emission (1995–2019), J. Cleaner Prod. 256 (2020), 120307.
[5] P.G. Pereirinha, M. González, I. Carrilero, D. Anseán, J. Alonso, J.C. Viera, Main trends and challenges in road transportation electrification, Transp. Res. Procedia 33 (2018) 235–242.
[6] M. Salvia, D. Reckien, F. Pietrapertosa, P. Eckersley, N.-A. Spyridaki, A. Krook-Riekkola, M. Olazabal, S. De Gregorio Hurtado, S.G. Simoes, D. Geneletti, V. Viguié, P.A. Fokaides, B.I. Ioannou, A. Flamos, M.S. Csete, A. Buzasi, H. Orru, C. de Boer, A. Foley, K. Rižnar, M. Matosović, M.V. Balzan, M. Smigaj, V. Baštáková, E. Streberova, N.B. Šel, L. Coste, L. Tardieu, C. Altenburg, E. K. Lorencová, K. Orru, A. Wejs, E. Feliu, J.M. Church, S. Grafakos, S. Vasilie, I. Paspaldzhiev, O. Heidrich, Will climate mitigation ambitions lead to carbon neutrality? An analysis of the local-level plans of 327 cities in the EU, Renew. Sustain. Energy Rev. 135 (2021) 110253, https://doi.org/10.1016/j.rser.2020.110253.
[7] F. Schreyer, G. Luderer, R. Rodrigues, R.C. Pietzcker, L. Baumstark, M. Sugiyama, R.J. Brecha, F. Ueckerdt, Common but differentiated leadership: strategies and challenges for carbon neutrality by 2050 across industrialized economies, Environ. Res. Lett. 15 (11) (2020), 114016.
[8] M. Yang, F. Yang, Net zero-carbon energy in rural China, Frontiers Journal of Renewable Energy 1 (1) (2020) 1–24.
[9] IEA (2020), Global EV Outlook 2020, IEA, Paris https://www.iea.org/reports/global-ev-outlook-2020.
[10] A. Das, A. Barai, I. Masters, D. Williams, Comparison of tab-to-busbar ultrasonic joints for electric vehicle Li-ion battery applications, World Electric Vehicle J. 10 (3) (2019) 55.
[11] M. Giansoldati, A. Monte, M. Scorrano, Barriers to the adoption of electric cars: Evidence from an Italian survey, Energy Policy 146 (2020) 111812, https://doi.org/10.1016/j.enpol.2020.111812.
[12] M. Xu, H. Yang, S. Wang, Mitigate the range anxiety: Siting battery charging stations for electric vehicle drivers, Transport. Res. Part C Emerg. Technolog. 114 (2020) 164–188.
[13] J. Zhang, T.-Q. Tang, Y. Yan, X. Qu, Eco-driving control for connected and automated electric vehicles at signalized intersections with wireless charging, Appl. Energy 282 (2021) 116215, https://doi.org/10.1016/j.apenergy.2020.116215.
[14] M. Eisel, I. Nastjuk, L.M. Kolbe, Understanding the influence of in-vehicle information systems on range stress–Insights from an electric vehicle field experiment, Transport. Res. Part F Traffic Psychol. Behaviour 43 (2016) 199–211.
[15] B.O. Varga, A. Sagoian, F. Mariasiu, Prediction of electric vehicle range: A comprehensive review of current issues and challenges, Energies 12 (5) (2019) 946.
[16] A.T. Thorgeirsson, M. Vaillant, S. Scheubner, F. Gauterin, Evaluating system architectures for driving range estimation and charge planning for electric vehicles, Software: Practice Experience 51 (1) (2021) 72–90.
[17] Weil M, Ziemann S, Peters J (2018) The issue of metal resources in Li-ion batteries for electric vehicles. In: Behaviour of lithium-ion batteries in electric vehicles. Springer, pp 59-74.
[18] Q. Zhang, C. Li, Y. Wu, Analysis of research and development trend of the battery technology in electric vehicle with the perspective of patent, Energy Procedia 105 (2017) 4274–4280.
[19] J. Deng, C. Bae, A. Denlinger, T. Miller, Electric vehicles batteries: requirements and challenges, Joule 4 (3) (2020) 511–515.
[20] A. Das, D. Li, D. Williams, D. Greenwood, Joining technologies for automotive battery systems manufacturing, World Electric Vehicle Journal 9 (2) (2018) 22.
[21] M.F.R. Zwicker, M. Moghadam, W. Zhang, C.V. Nielsen, Automotive battery pack manufacturing–a review of battery to tab joining, Journal of Advanced Joining Processes 1 (2020) 100017, https://doi.org/10.1016/j.jajp.2020.100017.
[22] W. Cai, in: Advances in Battery Manufacturing, Service, and Management Systems, John Wiley & Sons, Inc., Hoboken, NJ, USA, 2016, pp. 1–28, https://doi.org/10.1002/9781119060741.ch1.
[23] H. Saariluoma, A. Piiroinen, A. Unt, J. Hakanen, T. Rautava, A. Salminen, Overview of Optical Digital Measuring Challenges and Technologies in Laser Welded Components in EV Battery Module Design and Manufacturing, Batteries 6 (3) (2020) 47.
[24] P. Taheri, S. Hsieh, M. Bahrami, Investigating electrical contact resistance losses in lithium-ion battery assemblies for hybrid and electric vehicles, J. Power Sources 196 (15) (2011) 6525–6533.
[25] T. Solchenbach, P. Plapper, W. Cai, Electrical performance of laser braze-welded aluminum–copper interconnects, J. Manuf. Processes 16 (2) (2014) 183–189.
[26] L.N. Trinh, D. Lee, The Characteristics of Laser Welding of a Thin Aluminum Tab and Steel Battery Case for Lithium-Ion Battery, Metals 10 (6) (2020) 842.
[27] P. Wang, X. Chen, Q. Pan, B. Madigan, J. Long, Laser welding dissimilar materials of aluminum to steel: an overview, The International Journal of Advanced Manufacturing Technology 87 (9-12) (2016) 3081–3090.
[28] V. Dimatteo, A. Ascari, A. Fortunato, Continuous laser welding with spatial beam oscillation of dissimilar thin sheet materials (Al-Cu and Cu-Al): Process optimization and characterization, J. Manuf. Processes 44 (2019) 158–165.
[29] M. Fleckenstein, O. Bohlen, M.A. Roscher, B. Bäker, Current density and state of charge inhomogeneities in Li-ion battery cells with LiFePO4 as cathode material due to temperature gradients, J. Power Sources 196 (10) (2011) 4769–4778.
[30] S.D. Cramer, B.S. Covino (Eds.), Corrosion: Environments and Industries, ASM International, 2006, pp. 613–622, https://doi.org/10.31399/asm.hb.v13c.a0004170.
[31] M. Antler, Tribology of electronic connectors: Contact sliding wear, fretting, and lubrication, in: Electrical contacts, CRC Press, 1999, pp. 337–408.
[32] S.S. Lee, T.H. Kim, S.J. Hu, W. Cai, J.A. Abell, J. Li, Characterization of ultrasonic metal weld quality for lithium-ion battery tab joining, ASME J Manuf Sci Eng 135 (2) (2013), 021004.
[33] L.i. Shui, F. Chen, A. Garg, X. Peng, N. Bao, J. Zhang, Design optimization of battery pack enclosure for electric vehicle, Struct. Multidiscip. Optim. 58 (1) (2018) 331–347.
[34] M.J. Brand, E.I. Kolp, P. Berg, T. Bach, P. Schmidt, A. Jossen, Electrical resistances of soldered battery cell connections, J. Storage Mater. 12 (2017) 45–54.
[35] A. Das, D. Li, D. Williams, D. Greenwood, Weldability and shear strength feasibility study for automotive electric vehicle battery tab interconnects, J. Braz. Soc. Mech. Sci. Eng. 41 (1) (2019) 54.
[36] O. Mypati, D. Mishra, S. Sahu, S.K. Pal, P. Srirangam, A Study on Electrical and Electrochemical Characteristics of Friction Stir Welded Lithium-Ion Battery Tabs for Electric Vehicles, J. Electron. Mater. 49 (1) (2020) 72–87.
[37] J.P.M. Pragana, R.J.S. Baptista, I.M.F. Bragança, C.M.A. Silva, L.M. Alves, P.A. F. Martins, Manufacturing hybrid busbars through joining by forming, J. Mater. Process. Technol. 279 (2020) 116574, https://doi.org/10.1016/j.jmatprotec.2019.116574.
[38] Q. Zhang, R.C. Sekol, C. Zhang, Y. Li, B.E. Carlson, Joining lithium-ion battery tabs using solder-reinforced adhesive, J. Manuf. Sci. Eng. 141 (4) (2019).
[39] S. Dhara, A. Das, Impact of ultrasonic welding on multi-layered Al–Cu joint for electric vehicle battery applications: A layer-wise microstructural analysis, Mater. Sci. Eng., A 791 (2020) 139795, https://doi.org/10.1016/j.msea.2020.139795.
[40] X. Wu, T. Liu, W. Cai, Microstructure, welding mechanism, and failure of Al/Cu ultrasonic welds, J. Manuf. Processes 20 (2015) 321–331.
[41] J. Kundrat, Alexy M Batteries need strong connections-are resistance, laser and micro TIG welding the best suited joining technologies? In 2018 (2018) 97–114.
[42] Lee SS, Kim TH, Hu SJ, Cai WW, Abell JA (2010) Joining technologies for automotive lithium-ion battery manufacturing: A review. In, 2010 2010. American Society of Mechanical Engineers Digital Collection, pp 541-549.
[43] X. Chen, X. Wang, Z. Liu, Z. Hu, P. Huan, Q. Yan, N. Hiromi, Effect of Cu content on microstructure transformation and mechanical properties of Fe-Al dissimilar laser welded joints, Opt. Laser Technol. 126 (2020) 106078, https://doi.org/10.1016/j.optlastec.2020.106078.

[44] M.J. Brand, P.A. Schmidt, M.F. Zaeh, A. Jossen, Welding techniques for battery cells and resulting electrical contact resistances, J. Storage Mater. 1 (2015) 7–14.
[45] T.A. Mai, A.C. Spowage, Characterisation of dissimilar joints in laser welding of steel–kovar, copper–steel and copper–aluminium, Mater. Sci. Eng., A 374 (1–2) (2004) 224–233.
[46] S. Chen, Z. Zhai, J. Huang, X. Zhao, J. Xiong, Interface microstructure and fracture behavior of single/dual-beam laser welded steel-Al dissimilar joint produced with copper interlayer, The International Journal of Advanced Manufacturing Technology 82 (1-4) (2016) 631–643.
[47] A. Das, R. Fritz, M. Finuf, I. Masters, Blue laser welding of multi-layered AISI 316L stainless steel micro-foils, Opt. Laser Technol. 132 (2020) 106498, https://doi.org/10.1016/j.optlastec.2020.106498.
[48] M. Haubold, A. Ganser, T. Eder, M.F. Zäh, Laser welding of copper using a high power disc laser at green wavelength, Procedia CIRP 74 (2018) 446–449.
[49] Z. Sun, J.C. Ion, Laser welding of dissimilar metal combinations, J. Mater. Sci. 30 (17) (1995) 4205–4214.
[50] R.P. Shi, C.P. Wang, D. Wheeler, X.J. Liu, Y. Wang, Formation mechanisms of self-organized core/shell and core/shell/corona microstructures in liquid droplets of immiscible alloys, Acta Mater. 61 (4) (2013) 1229–1243.
[51] G. Phanikumar, S. Manjini, P. Dutta, K. Chattopadhyay, J. Mazumder, Characterization of a continuous CO 2 laser-welded Fe-Cu dissimilar couple, Metallurgical and Materials Transactions A 36 (8) (2005) 2137–2147.
[52] M. Velu, S. Bhat, Metallurgical and mechanical examinations of steel–copper joints arc welded using bronze and nickel-base superalloy filler materials, Mater. Des. 47 (2013) 793–809.
[53] S. Chen, J. Huang, J. Xia, H. Zhang, X. Zhao, Microstructural characteristics of a stainless steel/copper dissimilar joint made by laser welding, Metallurgical and Materials Transactions A 44 (8) (2013) 3690–3696.
[54] Z. Li, G. Fontana, M. Penasa, Autogenous laser welding of austenitic stainless steel to copper alloy, Sci. Technol. Weld. Joining 3 (2) (1998) 81–87.
[55] C. Yao, B. Xu, X. Zhang, J. Huang, J. Fu, Y. Wu, Interface microstructure and mechanical properties of laser welding copper–steel dissimilar joint, Opt. Lasers Eng. 47 (7-8) (2009) 807–814.
[56] S. Chen, J. Huang, J. Xia, X. Zhao, S. Lin, Influence of processing parameters on the characteristics of stainless steel/copper laser welding, J. Mater. Process. Technol. 222 (2015) 43–51.
[57] J. Li, Y. Cai, F. Yan, C. Wang, Z. Zhu, C. Hu, Porosity and liquation cracking of dissimilar Nd: YAG laser welding of SUS304 stainless steel to T2 copper, Opt. Laser Technol. 122 (2020) 105881, https://doi.org/10.1016/j.optlastec.2019.105881.
[58] S.V. Kuryntsev, A.E. Morushkin, A.K. Gilmutdinov, Fiber laser welding of austenitic steel and commercially pure copper butt joint, Opt. Lasers Eng. 90 (2017) 101–109.
[59] B.R. Moharana, S.K. Sahu, A. Maiti, S.K. Sahoo, T.K. Moharana, An experimental study on joining of AISI 304 SS to Cu by Nd-YAG laser welding process, Mater. Today:. Proc. 33 (2020) 5262–5268.
[60] B.R. Moharana, S.K. Sahu, S.K. Sahoo, R. Bathe, Experimental investigation on mechanical and microstructural properties of AISI 304 to Cu joints by CO2 laser, Engineering Science and Technology, an International Journal 19 (2) (2016) 684–690.
[61] Q. Nguyen, A. Azadkhou, M. Akbari, A. Panjehpour, A. Karimipour, Experimental investigation of temperature field and fusion zone microstructure in dissimilar pulsed laser welding of austenitic stainless steel and copper, J. Manuf. Processes 56 (2020) 206–215.
[62] S. RAMACHANDRAN, A.K. LAKSHMINARAYANAN, An insight into microstructural heterogeneities formation between weld subregions of laser welded copper to stainless steel joints, Transactions of Nonferrous Metals Society of China 30 (3) (2020) 727–745.
[63] H. Shen, M.C. Gupta, Nd: yttritium–aluminum–garnet laser welding of copper to stainless steel, J. Laser Appl. 16 (1) (2004) 2–8.
[64] M. Sahul, E. Tomčíková, M. Sahul, M. Pašák, B. Ludrovcová, E. Hodúlová, Effect of disk laser beam offset on the microstructure and mechanical properties of copper—AISI 304 stainless steel dissimilar metals joints, Metals 10 (10) (2020) 1294.
[65] M. Weigl, M. Schmidt, Influence of the feed rate and the lateral beam displacement on the joining quality of laser-welded copper-stainless steel connections, Physics Procedia 5 (2010) 53–59.
[66] G.R. Joshi, V.J. Badheka, Processing of bimetallic steel-copper joint by laser beam welding, Mater. Manuf. Processes 34 (11) (2019) 1232–1242.
[67] B. Mehlmann, A. Olowinsky, M. Thuilot, A. Gillner, Spatially Modulated Laser Beam Micro Welding of CuSn6 and Nickel-plated DC04 Steel for Battery Applications, J. Laser Micro/Nanoeng. 9 (3) (2014).
[68] Iqbal N, Nath S, Coleman AE, Lawrence J Parametric Study of Pulse Arc Welding (PAW) and Laser Beam Welding (LBW) Techniques for Electrical Vehicle Battery Cells. In, 2021. Trans Tech Publ, pp 611-617.
[69] Shaikh UF, Das A, Barai A, Masters I Electro-Thermo-Mechanical Behaviours of Laser Joints for Electric Vehicle Battery Interconnects. In, 2019 2019. IEEE, pp 1-6.
[70] M.J. Torkamany, S. Tahamtan, J. Sabbaghzadeh, Dissimilar welding of carbon steel to 5754 aluminum alloy by Nd: YAG pulsed laser, Mater. Des. 31 (1) (2010) 458–465.
[71] X. Cao, X. Zhou, Z. Li, Z. Luo, D. Ja, Interface microstructure and nanoindentation characterization of laser offset welded 5052 aluminum to press-hardened steel using a brass interlayer, Metals 9 (11) (2019) 1143.
[72] H. Okamoto, T.B. Massalski, Binary alloy phase diagrams, ASM International, Materials Park, OH, USA, 1990.
[73] L. Tricarico, R. Spina, D. Sorgente, M. Brandizzi, Effects of heat treatments on mechanical properties of Fe/Al explosion-welded structural transition joints, Mater. Des. 30 (7) (2009) 2693–2700.
[74] A. Mathieu, R. Shabadi, A. Deschamps, M. Suery, S. Matteï, D. Grevey, E. Cicala, Dissimilar material joining using laser (aluminum to steel using zinc-based filler wire), Opt. Laser Technol. 39 (3) (2007) 652–661.
[75] R. Indhu, S. Divya, M. Tak, S. Soundarapandian, Microstructure development in pulsed laser welding of dual phase steel to aluminium alloy, Procedia Manuf. 26 (2018) 495–502.
[76] Y. Jin, Y.-l. Li, H. Zhang, Microstructure and mechanical properties of pulsed laser welded Al/steel dissimilar joint, Trans. Nonferrous Metals Soc. China 26 (4) (2016) 994–1002.
[77] A.B. Pereira, A. Cabrinha, F. Rocha, P. Marques, F.A.O. Fernandes, R.J. Alves de Sousa, Dissimilar metals laser welding between DP1000 steel and aluminum alloy 1050, Metals 9 (1) (2019) 102.
[78] Q. Guan, J. Long, P. Yu, S. Jiang, W. Huang, J. Zhou, Effect of steel to aluminum laser welding parameters on mechanical properties of weld beads, Opt. Laser Technol. 111 (2019) 387–394.
[79] J. Ma, M. Harooni, B. Carlson, R. Kovacevic, Dissimilar joining of galvanized high-strength steel to aluminum alloy in a zero-gap lap joint configuration by two-pass laser welding, Mater. Des. 58 (2014) 390–401.
[80] R. Borrisutthekul, T. Yachi, Y. Miyashita, Y. Mutoh, Suppression of intermetallic reaction layer formation by controlling heat flow in dissimilar joining of steel and aluminum alloy, Mater. Sci. Eng., A 467 (1-2) (2007) 108–113.
[81] G. Pardal, S. Meco, S. Ganguly, S. Williams, P. Prangnell, Dissimilar metal laser spot joining of steel to aluminium in conduction mode, Int. J. Adv. Manufact. Technol. 73 (1-4) (2014) 365–373.
[82] S. Yan, Z. Hong, T. Watanabe, T. Jingguo, CW/PW dual-beam YAG laser welding of steel/aluminum alloy sheets, Opt. Lasers Eng. 48 (7-8) (2010) 732–736.
[83] F. Yan, X. Wang, F. Chai, H. Ma, L. Tian, X. Du, C. Wang, W. Wang, Improvement of microstructure and performance for steel/Al welds produced by magnetic field assisted laser welding, Opt. Laser Technol. 113 (2019) 164–170.
[84] N. LeBozec, A. LeGac, D. Thierry, Corrosion performance and mechanical properties of joined automotive materials, Mater. Corros. 63 (5) (2012) 408–415.
[85] J. Wloka, H. Laukant, U. Glatzel, S. Virtanen, Corrosion properties of laser beam joints of aluminium with zinc-coated steel, Corros. Sci. 49 (11) (2007) 4243–4258.
[86] Takehisa S, Iizuka T Galvanic Corrosion Related to Steel/Aluminum Dissimilar Joining Tailored Blank. In, 2014. Trans Tech Publ, pp 1460-1467.
[87] L. Jia, J. Shichun, S. Yan, N.i. Cong, C. junke, H. Genzhe, Effects of zinc on the laser welding of an aluminum alloy and galvanized steel, J. Mater. Process. Technol. 224 (2015) 49–59.
[88] S. Chen, J. Huang, K.e. Ma, H. Zhang, X. Zhao, Influence of a Ni-foil interlayer on Fe/Al dissimilar joint by laser penetration welding, Mater. Lett. 79 (2012) 296–299.
[89] D. Zhou, S. Xu, L.i. Peng, J. Liu, Laser lap welding quality of steel/aluminum dissimilar metal joint and its electronic simulations, Int. J. Adv. Manufact. Technol. 86 (5-8) (2016) 2231–2242.
[90] D. Zhou, S. Xu, L. Zhang, Y. Peng, J. Liu, Microstructure, mechanical properties, and electronic simulations of steel/aluminum alloy joint during deep penetration laser welding, Int. J. Adv. Manufact. Technol. 89 (1-4) (2017) 377–387.
[91] J. Yang, Z. Yu, Y. Li, H. Zhang, W. Guo, N. Zhou, Influence of alloy elements on microstructure and mechanical properties of Al/steel dissimilar joint by laser welding/brazing, Welding World 62 (2) (2018) 427–433.
[92] J. Sun, Q.i. Yan, W. Gao, J. Huang, Investigation of laser welding on butt joints of Al/steel dissimilar materials, Mater. Des. 83 (2015) 120–128.
[93] G. Sierra, P. Peyre, F.D. Beaume, D. Stuart, G. Fras, Steel to aluminium braze welding by laser process with Al–12Si filler wire, Sci. Technol. Weld. Joining 13 (5) (2008) 430–437.
[94] J. Yang, Y. Li, H. Zhang, W. Guo, D. Weckman, N. Zhou, Dissimilar laser welding/brazing of 5754 aluminum alloy to DP 980 steel: mechanical properties and interfacial microstructure, Metallurg. Mater. Trans. A 46 (11) (2015) 5149–5157.
[95] M.J. Zhang, G.Y. Chen, Y. Zhang, K.R. Wu, Research on microstructure and mechanical properties of laser keyhole welding–brazing of automotive galvanized steel to aluminum alloy, Mater. Des. 45 (2013) 24–30.
[96] H. Xia, X. Zhao, C. Tan, B.o. Chen, X. Song, L. Li, Effect of Si content on the interfacial reactions in laser welded-brazed Al/steel dissimilar butted joint, J. Mater. Process. Technol. 258 (2018) 9–21.
[97] P. Kah, C. Vimalraj, J. Martikainen, R. Suoranta, Factors influencing Al-Cu weld properties by intermetallic compound formation, Int. J. Mech. Mater. Eng. 10 (1) (2015) 1–13.
[98] M. Braunovic, Reliability of power connections, J. Zhejiang Univ.-SCIENCE A 8 (3) (2007) 343–356.
[99] S.J. Lee, H. Nakamura, Y. Kawahito, S. Katayama, Effect of welding speed on microstructural and mechanical properties of laser lap weld joints in dissimilar Al and Cu sheets, Sci. Technol. Weld. Joining 19 (2) (2014) 111–118.
[100] Y.Z. Liu, B.C. Zheng, Y.X. Jian, L. Zhang, Y.L. Yi, W. Li, Anisotropic in elasticity, sound velocity and minimum thermal conductivity of Al–Cu intermetallic compounds, Intermetallics 124 (2020) 106880, https://doi.org/10.1016/j.intermet.2020.106880.
[101] T. Solchenbach, P. Plapper, Mechanical characteristics of laser braze-welded aluminium–copper connections, Opt. Laser Technol. 54 (2013) 249–256.
[102] M. Braunovic, N. Alexandrov, Intermetallic compounds at aluminum-to-copper electrical interfaces: effect of temperature and electric current, IEEE Trans. Compon. Packag. Manuf. Technol. Part A: 17 (1) (1994) 78–85.

[103] D.i. Zuo, S. Hu, J. Shen, Z. Xue, Intermediate layer characterization and fracture behavior of laser-welded copper/aluminum metal joints, Mater. Des. 58 (2014) 357–362.
[104] F. Fetzer, M. Jarwitz, P. Stritt, R. Weber, T. Graf, Fine-tuned remote laser welding of aluminum to copper with local beam oscillation, Phys. Procedia 83 (2016) 455–462.
[105] F. Lerra, A. Ascari, A. Fortunato, The influence of laser pulse shape and separation distance on dissimilar welding of Al and Cu films, J. Manuf. Processes 45 (2019) 331–339.
[106] M.M. Hailat, A. Mian, Z.A. Chaudhury, G. Newaz, R. Patwa, H.J. Herfurth, Laser micro-welding of aluminum and copper with and without tin foil alloy, Microsyst. Technol. 18 (1) (2012) 103–112.
[107] Mys I, Schmidt M Laser micro welding of copper and aluminum. In, 2006 2006. International Society for Optics and Photonics, p 610703.
[108] Esser G, Mys I, Schmidt MHM Laser micro welding of copper and aluminium using filler materials. In, 2004 2004. International Society for Optics and Photonics, pp 337-342.
[109] M. Weigl, F. Albert, M. Schmidt, Enhancing the ductility of laser-welded copper-aluminum connections by using adapted filler materials, Phys. Procedia 12 (2011) 332–338.
[110] Y. Hu, X. He, G. Yu, Z. Ge, C. Zheng, W. Ning, Heat and mass transfer in laser dissimilar welding of stainless steel and nickel, Appl. Surf. Sci. 258 (15) (2012) 5914–5922.
[111] Zhang X, Kobayashi N, Motegi Y, Yade N Porosity suppression in laser welding of pure nickel and stainless steel. In, 2013. Laser Institute of America, pp 289-293.
[112] Z. Li, G. Yu, X. He, S. Li, Y. Zhao, Numerical and experimental investigations of solidification parameters and mechanical property during laser dissimilar welding, Metals 8 (10) (2018) 799.